



**Titre:** A 9.2-ns to 1- $\mu$ s digitally controlled multituned deadtime optimization for efficient GaN HEMT power converters

**Auteurs:** Mousa Karimi, Mohamed Ali, Amir Aghajani, Ahmad Hassan, Mohamad Sawan, & Benoit Gosselin

**Date:** 2022

**Type:** Article de revue / Article

**Référence:** Karimi, M., Ali, M., Aghajani, A., Hassan, A., Sawan, M., & Gosselin, B. (2022). A 9.2-ns to 1- $\mu$ s digitally controlled multituned deadtime optimization for efficient GaN HEMT power converters. IEEE Transactions on Circuits and Systems I: Regular Papers, 69(11), 4381-4394. <https://doi.org/10.1109/tcsi.2022.3187105>

 **Document en libre accès dans PolyPublie**

Open Access document in PolyPublie


**URL de PolyPublie:** <https://publications.polymtl.ca/51255/>

PolyPublie URL:

**Version:** Version finale avant publication / Accepted version  
Révisé par les pairs / Refereed

**Conditions d'utilisation:** Tous droits réservés / All rights reserved

Terms of Use:

 **Document publié chez l'éditeur officiel**

Document issued by the official publisher

**Titre de la revue:** IEEE Transactions on Circuits and Systems I: Regular Papers (vol. 69, no. 11)

Journal Title:

**Maison d'édition:** IEEE

Publisher:

**URL officiel:** <https://doi.org/10.1109/tcsi.2022.3187105>

Official URL:

**Mention légale:** © 2022 IEEE. Personal use of this material is permitted. Permission from IEEE must be obtained for all other uses, in any current or future media, including reprinting/republishing this material for advertising or promotional purposes, creating new collective works, for resale or redistribution to servers or lists, or reuse of any copyrighted component of this work in other works.

Legal notice:

# A 9.2-ns to 1- $\mu$ s Digitally Controlled Multituned Deadtime Optimization for Efficient GaN HEMT Power Converters

Mousa Karimi<sup>ID</sup>, *Member, IEEE*, Mohamed Ali<sup>ID</sup>, *Member, IEEE*, Amir Aghajani, Ahmad Hassan<sup>ID</sup>, *Member, IEEE*, Mohamad Sawan<sup>ID</sup>, *Fellow, IEEE*, and Benoit Gosselin<sup>ID</sup>, *Member, IEEE*

**Abstract**—This paper presents a tunable new deadtime control circuit providing an optimal delay for power converter optimization. Our method can reduce the deadtime loss while improving the efficiency and power density of a given power converter. The circuit presents a reconfigurable delay element to generate a wide range of deadtime for different power conversion applications with varying loads and input voltages. The optimal deadtime equation for buck converters is derived, and its dependency on the input voltage and load is discussed. Experimental results show that the presented circuit can provide a wide range of deadtime delays, ranging from 9.2 ns to 1000 ns. The power consumption of the presented circuit is measured for different capacitive loads ( $C_L$ ) and operating frequencies ( $f_s$ ). The circuit consumed a power between 610  $\mu$ W and 850  $\mu$ W across the measured deadtime ranges while  $C_L = 12$  pF,  $V_{dd} = 3.3$  V, and  $f_s = 200$  kHz. The proposed deadtime generator can operate up to 18 MHz when the minimum deadtime of 9.2 ns is selected. The presented circuit occupies an area of  $150\mu\text{ m} \times 260\mu\text{ m}$ . The fabricated chip is connected to a buck converter to validate the operation of the proposed circuit. The efficiency of a typical buck converter with minimum  $T_{DLH}$  and optimal  $T_{DHL}$  at  $I_{Load} = 25$  mA is improved by 12% compared to a converter with a fixed deadtime of  $T_{DLH} = T_{DHL} = 12$  ns.

**Index Terms**—Power converters, gate driver, GaN HEMT transistors, optimized deadtime control, efficiency, adjustable circuit, power consumption, load variation, different input voltage.

Manuscript received 7 December 2021; revised 18 May 2022; accepted 22 June 2022. This work was supported in part by the Natural Sciences and Engineering Research Council of Canada, in part by the Mathematics of Information Technology and Complex Systems (MITACS), in part by CMC Microsystems, in part by the Quebec Strategic Alliance in Microsystems (ReSMiQ), and in part by the Canada Research Chair in Smart Biomedical Microsystems. This article was recommended by Associate Editor M. Barragan. (*Corresponding author: Mousa Karimi.*)

Mousa Karimi, Amir Aghajani, and Benoit Gosselin are with the Smart Biomedical Microsystems Laboratory, Université Laval, Quebec, QC G1V 0A6, Canada (e-mail: mousa.karimi.1@ulaval.ca).

Mohamed Ali is with the Polystim Neurotechnology Laboratory, Department of Electrical Engineering, Polytechnique Montréal, Montreal, QC H3T 1J4, Canada, and also with the Department of Microelectronics, Electronics Research Institute, Cairo 12622, Egypt.

Ahmad Hassan is with the Polystim Neurotechnology Laboratory, Department of Electrical Engineering, Polytechnique Montréal, Montreal, QC H3T 1J4, Canada.

Mohamad Sawan is with the Polystim Neurotechnology Laboratory, Department of Electrical Engineering, Polytechnique Montréal, Montreal, QC H3T 1J4, Canada, and also with the CenBRAIN Laboratory, School of Engineering, Westlake University, Hangzhou 310024, China.

Color versions of one or more figures in this article are available at <https://doi.org/10.1109/TCSI.2022.3187105>.

Digital Object Identifier 10.1109/TCSI.2022.3187105

## I. INTRODUCTION

EFFICIENT power converters are essential circuits used in System-in-Packages (SiP) modules for distributing power to the different building blocks [1]. Many high-performance applications, such as video processing [2], are particularly power-hungry. Power converters are ubiquitous in industrial and consumer electronics. They are employed in so many applications, from smartphones, tablets, and headphones [3], [4], to TV sets, car electronics, wireless power chargers for electric vehicle [5], [6], public fitness equipment [7], and wearable medical devices [8]. Power converters, such as DC–DC converters, bridges (half and full), and class-D power amplifiers, must present high efficiency and power density [9]–[12]. A thorough analysis of losses must be performed, so a power converter design can meet these key criteria [13]–[15]. Losses must be examined at the component and peripheral circuits levels to improve converter performance. Si MOS, SiC MOS, and GaN transistors are the most frequently used power switches in power converters [16]–[20]. A Figure of Merit (FoM) =  $Q_{OSS}R_{ON}$  is recommended in [21] to the advantage of GaN's over Si or SiC ( $Q_{OSS}$  and  $R_{ON}$  are the output capacitor charge and the on-resistance of the power switch, respectively). Furthermore, the GaN transistor does not suffer from reverse recovery loss due to the absence of a body diode, has a lower gate charge, and a smaller output capacitance than with Si or SiC [22], [23]. The carrier mobility in the 2D electron gas (2DEG) channel is considerably faster in the GaN transistor, and the breakdown voltage is higher due to its large acute electric field [24], [25]. Hence, GaN transistors are excellent candidates for ultra-high-power density operation. Fig. 1 shows the different types of losses found in power converters. Fig. 1(a) depicts a simplified schematic of a conventional power converter. Fig. 1(b) illustrates the power converter's essential waveforms needed for the case of GaN transistors. In contrast, Fig. 1(c) shows the needed power converter's waveforms when the power switches are implemented with Si MOSFETs.

The rise and fall times ( $t_r$  and  $t_f$ ) of the main curve of the power converter ( $V_{sw}$ ) are shorter when GaN transistors are used, as shown in Figs. 1(b) and 1(c). In the same condition, the switching time of the GaN transistors is six times faster than for Si MOSFET [24]. Accordingly, the switching losses ( $P_{sw}$ ) of the GaN transistors are minimized because the overlap of  $I_{DS}$  and  $V_{DS}$  of the high-side power switch (HSS)

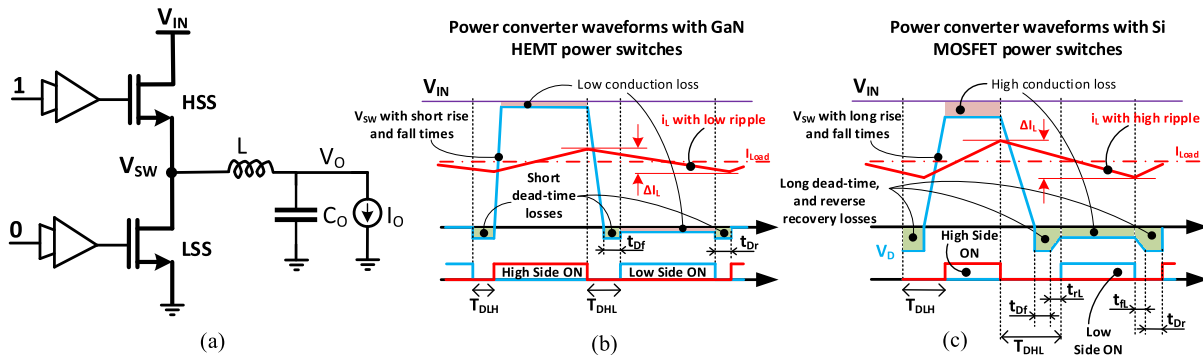


Fig. 1. Conventional power converter. (a) Simplified schematic, (b) waveforms with GaN HEMT power switches, and (c) waveforms with Si MOSFET power switches.

is minimized when the  $t_r$  and  $t_f$  of  $V_{SW}$  are shorter [24]. Figs. 1(b) and 1(c) show that the power converter using GaN transistors has a significantly lower conduction loss ( $P_{CON}$ ). The  $P_{CON}$  equals the value of  $R_{ON}$  times the value of the RMS current of the power switches (see the Appendix for more details). GaN transistors achieve lower conduction loss because their  $R_{ON}$  is smaller than that of Si MOSFETs. Another type of loss in power converters is due to the reverse recovery charge ( $Q_{RR}$ ) in the freewheeling of the low-side switch (LSS). This loss equals the multiplication of  $Q_{RR}$ ,  $V_{IN}$ , and the operating frequency ( $f_s$ ) of the converter (see the Appendix). Moreover, this loss can be significant in power converters with Si MOSFETs. However, the loss is almost zero in GaN-based converters because the GaN is a majority carrier device, and it does not have reverse recovery-based loss. This point is clarified in Figs. 1(b) and 1(c) for Si and GaN-based converters, respectively. Another factor that contributes to the switching loss is the stored energy in the output capacitance of the power switch, which is dissipated during the turn-on time. This loss ( $P_{CAP}$ ) depends on the output charge of the power switch ( $Q_{OSS}$ ) and equals the multiplication of  $Q_{OSS}$ ,  $f_s$ , and  $V_{IN}$  (see the Appendix). GaN devices also have small output capacitances compared with Si MOSFETs. Accordingly, they exhibit a much smaller  $P_{CAP}$ . The LSS body diode in power converters can conduct during the deadtime, resulting in a power loss associated with the forward voltage of the diode. Although GaN devices have no body diode, their symmetry helps in conducting in the third quadrant with a diode-like behavior. The lateral GaN structure is comprised of a source and drain that are linked by a 2DEG channel, with the Gate controlling the conductivity of the 2DEG. Figs. 2(a) and 2(b) illustrate the cross-sectional view of the lateral structure of a GaN transistor and its behavior in the first and third quadrants, respectively. When the current flows in reverse conduction in GaN devices, the drain and source terminals can swap the termination. GaN transistors have a high third quadrant conduction (e.g.,  $V_{SD}$  of 2 V at 10 A for LMG5200 compared to  $\sim 1$  V for Si MOSFETs). Hence, GaN devices typically exhibit a higher power loss during deadtime ( $P_{DT}$ ). This power loss can be calculated as follows:

$$P_{DT} = f_s \times V_{SD} \times I_{OUT} \times (T_{DLH} + T_{DHL}), \quad (1)$$

where  $I_{OUT}$  is the output current of the power converter; and  $T_{DLH}$  and  $T_{DHL}$  are the required deadtimes, as shown

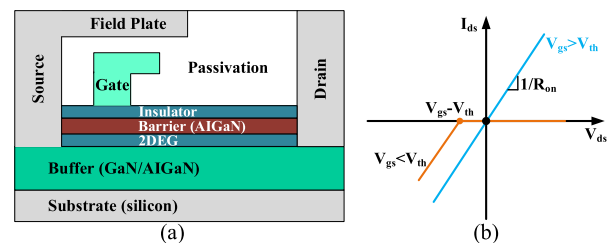


Fig. 2. GaN transistor: (a) Cross section of the lateral structure, (b) simplified behavior in 1<sup>st</sup> and 3<sup>rd</sup> quadrant.

in Figs. 1(b) and 1(c). Accordingly, an adjustable deadtime control circuit is necessary to select the optimal deadtime for different power converter applications to achieve maximum efficiency. When the optimum deadtime is tuned, the signal of  $V_{SW}$  (Fig. 1 (a)) has sufficient time to reach zero, but does not cross it. Then, the buck converter can work at its maximum operating frequency and maximum efficiency. The other power converter losses to consider include those resulting from the gate driver ( $P_G$ ), output inductor DC resistance ( $P_{DCR}$ ), equivalent series resistance of the output capacitance ( $P_{ESR}$ ), and power switch packaging losses (see Appendix) [26]–[30].

The gate driver supply voltage ( $V_{DC}$ ) is usually separated from the power switches supply ( $V_{IN}$ ) in power converter implementation where two n-channel bootstrapped power switches are used as HSS and LSS (Fig. 3(a)). The  $V_{DC}$  is fixed to +5 V, while the  $V_{IN}$  is between 12 V and 200 V depending on the application. Accordingly, the same gate driver design would support different power converter applications. The amount of deadtime delay required to activate the HSS and LSS switches, which depends on the value of  $V_{IN}$ , must be set to longer values because the operation of power switches is known to be slower at higher  $V_{IN}$ . A gate driver with a reconfigurable deadtime control circuit allows to finetune and find the optimal the required deadtime for various  $V_{IN}$ . This mechanism ensures a power converter design with a sound efficiency performance for a wide range of applications with different  $V_{IN}$  values [31], [32].

The needed power converter deadtime depends on the type of load (RLC, RL, and LC) and the values of the used off-chip passive components. The primary distinction among most converter types (DC–DC, Class-D power amplifiers, and bridges, including half and full) is the kind of load. Accordingly, adopting a single implementation of a gate driver

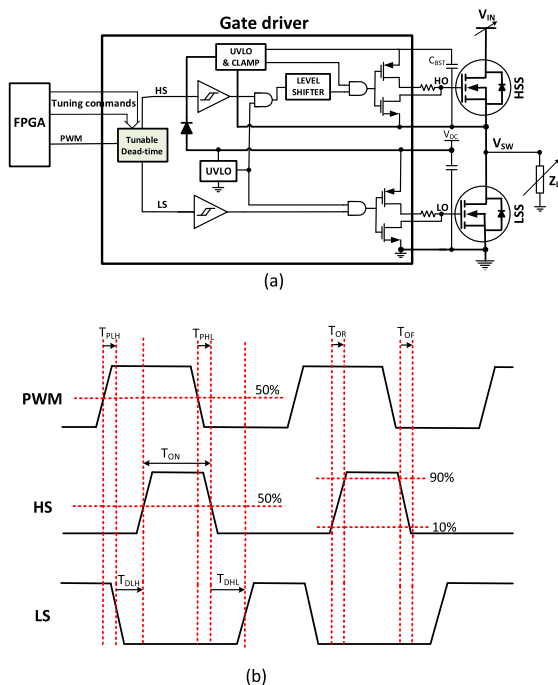


Fig. 3. (a) A power converter with a tunable dead-time generator, and (b) timing diagram of gate driver in PWM mode under no load condition.

with a tunable deadtime delay for the various power converter topologies has several benefits. Fig. 3(a) shows a power converter with variable input voltage ( $V_{IN}$ ), variable load ( $Z_L$ ), and reconfigurable deadtime control fulfilled with a gate driver [33]–[38]. In this configuration, a field-programmable gate array (FPGA) sends the tuning commands to the deadtime control circuit. Fig. 3(b) shows the timing diagram of the gate driver with a PWM signal under no load condition where the switching specifications are illustrated, including the turn-off delay ( $T_{PHL}$ ), turn-on delay ( $T_{PLH}$ ), output rise time ( $T_{OR}$ ), output fall time ( $T_{OF}$ ), low-to-high transition deadtime ( $T_{DLH}$ ), and high-to-low transition deadtime ( $T_{DHL}$ ).

The deadtime control circuit is a key circuit in gate drivers that enables high-quality switching to drive the HSS and LSS power switches [39], [40]. Fig. 3(a) presents a general building block of a power converter that includes a gate driver associated with an integrated deadtime control circuit [41]. Although the gate driver implementation frequently has a fixed deadtime, a reconfigurable gate driver with the ability to adjust the deadtime delay is desirable to provide an optimal deadtime to reduce  $P_{DT}$ , thereby increasing the efficiency and power density [42]–[45].

Several tunable deadtime control circuits were discussed in the literature. The use of a gate driver with adjustable deadtime delay used for tuning a half-bridge with a high supply voltage ( $V_{IN} = +86$  V) is discussed in [36]. This gate driver configuration generates a variable deadtime delay between 4.5 ns and 58 ns for a variable load with a current ranging from 200 mA to 2 A. However, this deadtime circuit does not generate enough delays (i.e. longer delays are required) to support power converters with high  $V_{IN}$  and wider load range. A commercial gate driver integrated circuit with tunable deadtime delay is presented in [37]. It drives a half-bridge that can operate up to  $V_{IN} = 200$  V and supply up to 3 A

to a load. However, the deadtime control involved in this gate driver uses two off-chip resistors to allow a tunable operation. This situation increases the power dissipation of the gate driver. Moreover, the reliability of the gate driver circuit can be affected, and the resolution of the deadtime delay can be degraded.

A deadtime optimization method for GaN-based buck converters is described in [42]. In this paper, the optimization relies on mathematical analysis and the derived equations for both  $T_{DLH}$  and  $T_{DHL}$ . In [42], an efficiency improvement of up to 4.5% is achieved compared to using a fixed deadtime, but one drawback with the derived equations is a lack of accuracy. A digital deadtime correction wherein the deadtime can be tuned during a power converter operation is reported in [46]. In this technique, the deadtime circuit measures the voltages of  $V_{SW}$  and LSS gate and tunes the deadtime. An adaptive deadtime control methodology wherein a digital circuit was used to optimize the required deadtime through measuring the voltage of  $V_{SW}$  is presented in [47]. Comparator-based, dual-edge modulation deadtime optimization, and adaptive deadtime controller techniques, are presented in [48], [49], and [50], respectively. An issue with the deadtime control circuits presented in [45]–[50] is that the sensing voltage  $V_{SW}$  for estimating the required deadtime needs a few switching cycles of the power converter operation because the  $V_{SW}$  signal has the longest rise and fall times ( $t_r$  and  $t_f$ ) in the power converter. This is decreasing the performance of the deadtime control circuit. The additional circuit required to measure the potential of  $V_{SW}$  can also affect the power density and increase the cost. A dynamic deadtime optimization technique for a power converter is presented in [51]. In this approach, an additional circuit was placed in parallel with the LSS, which affects the performance of LSS. Another circuit is also needed to sense the voltage of  $V_{IN}$ , which increases the overall power consumption of the converter and reduces the efficiency.

In this work, we propose a novel circuit for deadtime control that provides a wide range of delays to the power converter HS and LS by utilizing three independent reconfigurable analog modules. The tunable modules can receive digital commands from a controller to tune the required deadtime. In contrast with what is usually accepted, i.e. the values of  $T_{DHL}$  and  $T_{DLH}$  must be minimized as much as possible according to (1) to decrease the deadtime loss, we show that this applies only for  $T_{DLH}$ , while an optimal value can be reached for  $T_{DHL}$  to decrease the power converter's deadtime loss. Indeed, if the  $T_{DHL}$  is made shorter or longer than the optimal value, the deadtime loss increases degrading the converter efficiency. The remaining of this paper is arranged as follows. Section II presents the proposed building blocks, circuit implementations, and mathematical analyses. Section III presents the experimental results. Section IV discusses the performance comparison with other solutions. Section V provides the conclusion.

## II. PROPOSED TUNABLE DEADTIME CIRCUIT

### A. Proposed Architecture

Fig. 4 illustrates the configuration of the proposed Wide Range Multi-Tuned-Deadtime Control Circuit (WRM-TDC). Three adjustable parts (A, B, and C) are utilized to allow a wide range of deadtime delays. The controller command can be used to set up these parts (32 dedicated switches are used

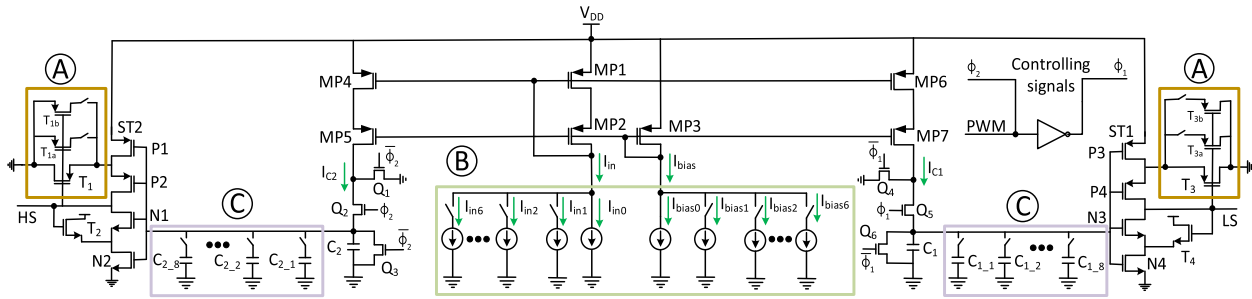


Fig. 4. Schematic of the proposed Multi-tuned-dead-time generator. Three tunable parts of A, B, and C can receive tuning commands from the FPGA to reconfigure the circuit for creating different required delays between the generated non-overlapping signals on the outputs of HS and LS [40]. All the components of the proposed circuit will be integrated as a part of gate driver for different power converter applications.

for both sides). The presented WRM-TDC uses two initial capacitors ( $C_1$  and  $C_2$ ), which are linearly charged by  $I_{C1}$  and  $I_{C2}$ , respectively, to produce two rectangular signals.

These rectangular waveforms are applied to two Schmitt Triggers (ST1 and ST2). Two pulse signals are generated at the output of ST1 and ST2 when the rectangular signals are applied because the hysteresis windows of ST<sub>1</sub> and ST<sub>2</sub> are initialized (switching thresholds of STs are set with initial values). The two pulse-shaped signals produced at the output of STs do not overlap each other due to the created deadtime between  $T_{DLH}$  and  $T_{DHL}$  thanks to the presented WRM-TDC. A wide swing current source (MP1-MP7) is employed to mirror the currents of  $I_{in}$  and  $I_{bias}$  (for producing  $I_{C1}$  and  $I_{C2}$ ). In addition, the switches of  $Q_1$ - $Q_6$  are closed/opened with controlling signals  $\phi_1$  and  $\phi_2$  to charge/discharge  $C_1$  and  $C_2$ . The gate driver with the adjustable deadtime receives a PWM signal from the controller and generates two waveforms for HS and LS power switches with optimal  $T_{DLH}$  and  $T_{DHL}$  to allow for high power conversion efficiency with minimized deadtime loss.

The advantages of the presented WRM-TDC are:

- Digital commands are sent to the WRM-TDC to adjust the required deadtime of the gate driver. Accordingly, off-chip components or digital-to-analog converters are not needed. Therefore, the communication between the FPGA and the gate driver is facilitated, the power consumption of the gate driver is decreased, and the reliability of power converters is increased. In addition, the strategy for generating different deadtimes is simple and fast.
- To tune the proposed deadtime control circuit, we use three different current/capacitor-based tuning circuits (A, B, and C). Hence, producing a wide range of  $T_{DLH}$  and  $T_{DHL}$  is possible. This potential procedure is essential for power converters with various loads and  $V_{IN}$ .
- The type of circuits used to design each reconfigurable part is different. Accordingly, the attained resolution from each part is different. ST has the highest resolution, while the capacitor-based parts have the lowest resolution. This situation allows the allocation of the least significant bits (LSBs) of the controlling code to ST-based tuning circuit. Meanwhile, the most significant bits (MSBs) are dedicated to the capacitor-based parts. Therefore, when large deadtimes is required, the proposed WRM-TDC can support power converters with a wide range of  $V_{IN}$  and load.

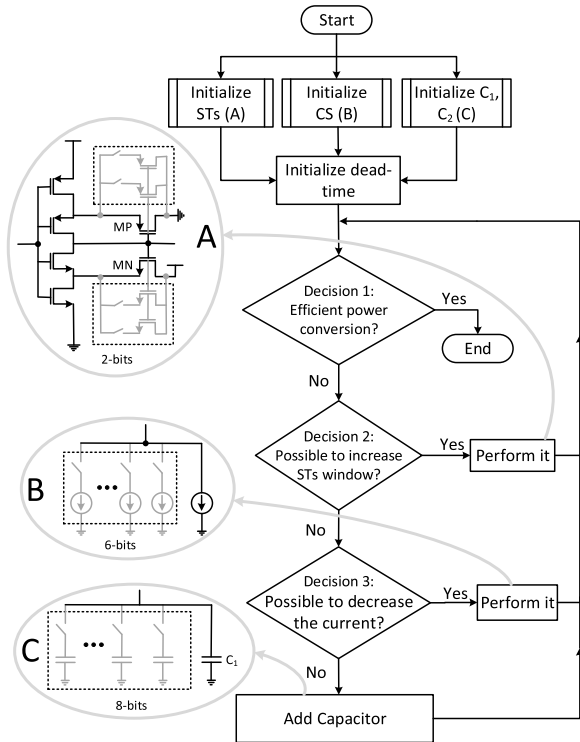


Fig. 5. Flowchart of the operation of proposed deadtime control circuit.

### B. Circuit Programming and Optimization Approach

Fig. 5 clarifies the flexibility and the reconfigurability of the presented WRM-TDC. The involved parameters and the methodologies used to realize the projected objectives are illustrated. Three sections of A, B, and C must be initiated to start the deadtime. Then, the power conversion must be verified according to the decision steps of the flowchart (i.e. decision 1, decision 2, and decision 3) to achieve maximum efficiency in a given power converter. According to [17], an efficient conversion occurs when the power converter output waveform ( $V_{SW}$ ) meets the following conditions:  $t_{Df} = 0$ ,  $t_{Dr} = 0$ ,  $t_{rL} = 0$ , and  $t_{fL} = 0$ . The power dissipation (conduction loss) of the transistor increases with  $V_{DS}$ . During “ $t_{Df}$ ” and “ $t_{rL}$ ” ( $t_{fL}$  and  $t_{Dr}$ ) the voltage drop across the low side transistor ( $V_{DS}$ ) and is larger than that when the low side transistor is ON. This increases the conduction loss of

the low side transistor during the “ $t_{Df}$ ” and “ $t_{rL}$ ” ( $t_{fL}$  and  $t_{Dr}$ ). Thus, by minimizing the “ $t_{Df}$ ” and “ $t_{rL}$ ” ( $t_{fL}$  and  $t_{Dr}$ ), the conduction loss of the low-side transistor will be minimized, and the power conversion efficiency will be maximized.

If the conversion is efficient, then the configured WRM-TDC is convenient for the application. Otherwise, the first tuning part (A) must be reconfigured to achieve more delays if there is still some bit available for the reconfiguration of part A. Then, the status of the power converter must be verified again to determine if the target efficiency has been met. To reconfigure part A, 2 bits are dedicated to change the values of  $T_{DLH}$  and  $T_{DHL}$ . As shown in Fig. 5 (part A), MOSFETs are adding in parallel with MP step by step and the same for MN to change the deadtimes. Consequently, the  $V_{ref}$ s of STs will be modified, resulting in a broader hysteresis window being applied to the ramp signals over the main capacitors. Finally, the deadtime is increased to reach the optimal deadtime.

If the conversion is still inefficient when both bits of part A are used, then part B must be configured, as shown in Fig. 5. Part B utilizes a tunable current source that is controlled by 6 bits. The amount of delivered current to the main capacitors must be decreased to obtain more deadtime. For this purpose, the number of paralleled current sources must be decreased step by step, with the condition of “efficient conversion” being verified at every step. If all the 6 bits of part B were used, then the third part (C), which contains a capacitive bank, must be included in the circuit. The capacitive bank is controlled with 8 bits to adjust the capacitor value and tune the adequate deadtime for the power converter based on the values of  $V_{IN}$  and the load. If all the 16 bits of parts A, B, and C were used, and the converter still needed longer deadtime, then the values of  $V_{IN}$  and the load should be fixed. Specifically, the proposed reconfigurable deadtime can be useful over specified ranges of  $V_{IN}$  and loads. Notably, cases where  $I_{OUT}$  is high, and  $V_{IN}$  is low require short deadtimes.

### C. Circuit Implementation

Fig. 6 shows the circuit implementation of the reconfigurable parts (A, B, and C) of the proposed WRM-TDC. In part A,  $T_1$  and  $T_3$  are the key transistors to configure the hysteresis windows of ST2 and ST1, respectively. These hysteresis windows of ST1 and ST2 depend on the dimensions of  $T_1$  and  $T_3$ , respectively. Two p-channel MOSFETs of  $T_{1a}$  and  $T_{1b}$  ( $T_{3a}$  and  $T_{3b}$ ) are included in parallel with  $T_1$  ( $T_3$ ) to design an adjustable part on the STs. The hysteresis windows of the STs can be expanded if their adjusting transistors are excluded from the STs. Hence, the p-channel MOSFETs ( $T_{1a}$ ,  $T_{3a}$ ,  $T_{1b}$ , and  $T_{3b}$ ) are enabled to achieve the shortest possible deadtime as the initial configuration. Then, this adjusting part A must be excluded from the circuit by active low switches (p-type transistors) to obtain the longer deadtime.

$T_{1b}$  and  $T_{3b}$  which are tunable parts of ST2 and ST1, respectively, are controlled with the activating bits of  $b_{0L}$  and  $b_{0H}$  to change the values of the delays of  $T_{DLH}$  and  $T_{DHL}$  (the same for  $T_{1a}$  and  $T_{3a}$ ).

The second tunable parts are  $I_{in}$  and  $I_{bias}$ . The parallel diode connected n-channel MOSFETs of MN0–MN13 are implemented to fulfill this part with real circuits. The values of the produced  $T_{DLH}$  and  $T_{DHL}$  are inversely related with currents  $I_{in}$  and  $I_{bias}$ . Accordingly, all the diodes connected

TABLE I  
DIMENSIONS OF ALL COMPONENTS ADOPTED  
FOR REALIZING THE CIRCUIT

	Comp.	P1,2;N1,2	T2	T1	T1a	T1b
A, ST	W( $\mu$ m)	0.4	0.6	0.6	0.8	1
	L( $\mu$ m)	0.45	0.35	0.35	0.35	0.35
C	Comp.	$C_2$	$C_{2-1}$	$C_{2-2}$	$C_{2-3}$	$C_{2-4}$
	Value(fF)	10	15	30	60	120
	Comp.	$C_{2-5}$	$C_{2-6}$	$C_{2-7}$	$C_{2-8}$	
	Value(pF)	0.24	0.5	1	1.5	
B	Comp.	MN0	MN1	MN2	MN3	MN4
	W( $\mu$ m)	0.4	0.6	0.8	1	1.2
	L( $\mu$ m)	5	5	5	5	5
	Comp.	MN5	MN6	N/A	N/A	N/A
	W( $\mu$ m)	1.4	1.4	N/A	N/A	N/A
	L( $\mu$ m)	5	5	N/A	N/A	N/A
CS	Comp.	MP1, MP2	MP3	MP4- MP7	All switches	
	W( $\mu$ m)	0.8	0.4	0.8	0.4	
	L( $\mu$ m)	0.35	0.35	0.35	0.35	

N/A= NON-APPLICABLE; ST: SCHMITT TRIGGER; MP, P, N, T, MN: ARE TAGGED ON FIG 4,6; CS: WIDE SWING CURRENT SOURCE.

must be added in the circuit to achieve the minimum  $T_{DLH}$  and  $T_{DHL}$ . Then, the MN1–MN6 and MN8–MN13 must be removed from the circuit with the active low switches (p-type transistor) to provide longer delays.

The third reconfigurable part of the proposed WRM-TDC is shown in part C. The value of the produced  $T_{DLH}$  and  $T_{DHL}$  are in direct relation with the sizes of the capacitors used. Accordingly, one capacitor is utilized in the circuit as initialization to attain the shortest  $T_{DLH}$  and  $T_{DHL}$ . Then, the integrated capacitors ( $C_{1-1} - C_{1-8}$  and  $C_{2-1} - C_{2-8}$  in Fig. 6) are included in the circuit to be in parallel with the main capacitors ( $C_1$  and  $C_2$  in Fig. 4) for creating longer  $T_{DLH}$  and  $T_{DHL}$ . The integrated switches in this part must be active high type (n-type MOSFET).

The aspect ratios of the transistors and the values of the passive components used to implement each part of the presented circuit are listed in Table I. These components are needed for implementing one side of the circuit (generating  $T_{DHL}$ ). The other side of the circuit uses the same components to generate  $T_{DLH}$ . 32 bits  $b_{0L}$  to  $b_{15L}$  and  $b_{0H}$  to  $b_{15H}$  are devoted for controlling the 32 switches used to realize the tunable parts in both sides of Fig. 4. Among these 32 bits, four LSB bits of  $b_{0L}$ - $b_{1L}$  and  $b_{0H}$ - $b_{1H}$  are allocated to the ST-based parts (in the right and left of Fig. 4), 12 bits of  $b_{2L} - b_{7L}$  and  $b_{2H} - b_{7H}$  are earmarked to current source part ( $I_{in}$  and  $I_{bias}$ ), and the 16 MSB bits of  $b_{8L} - b_{15L}$  and  $b_{8H} - b_{15H}$  are assigned to capacitor-based tunable part.

The created delays in the presented WRM-TDC depends on the amounts of currents  $I_{C1}$  and  $I_{C2}$  (Fig. 4) delivered by the current source to the integrated capacitors. Given the relation between the output current and the values of  $I_{in}$  and  $I_{bias}$ , the operation of the proposed design against mismatch and process corners should be validated. Specifically, MN0–MN13 (Fig. 6, part B), which are used to adjust the biasing current, must be made robust against process variations. The operations on both sides of the proposed WRM-TDC are the same during the production of  $T_{DHL}$  and  $T_{DLH}$  (deadtime). A different deadtime is due to the various parameter values on each

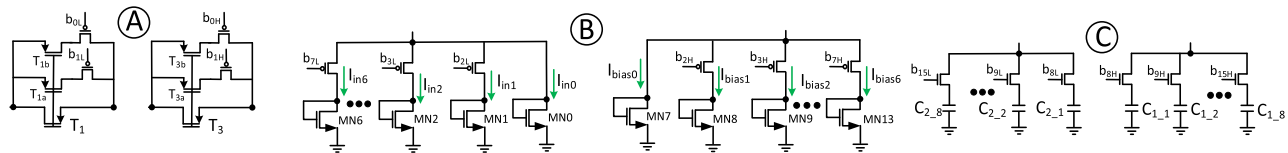


Fig. 6. Transistor level implementation of the tunable A, B, and C parts.

side of the circuit. Accordingly, the circuit is evaluated to be robust against process variations for one of the deadtimes (i.e.,  $T_{DHL}$ ). The simulated deadtime value  $T_{DHL}$  is 47.5 ns for the designed circuit and associated typical case corner (i.e., typical NMOS and PMOS transistors and  $V_{DD} = 3.3$  V). A worst-case scenario is simulated to anticipate the effect of process variations. Using the AMS kit, “fast NMOS/fast PMOS” yields the highest power consumption or Worst power (WP), whereas “slow NMOS/slow PMOS” yields the slowest speed or Worst speed (WS). In this study, we evaluate the operation of the proposed circuit in the WP and WS cases for one of the tuning commands (i.e., 0FFF). The WP and WS are the worst operating conditions of the circuit (Fig. 6). The simulated deadtime values  $T_{DHL}$  for the WP and WS cases are 35.8 and 72.92 ns, respectively. The WS case yields the longest deadtime, while the WP has the shortest deadtime. The impact of the process variations on the performance of the proposed WRM-TDC is studied using a Monte-Carlo simulation. A supply voltage of  $V_{DD} = 3.3$  V is set for the simulation. The results for  $T_{DHL}$  are shown in Fig. 7 (a). Specifically, the simulated  $T_{DHL}$  shows a log-normal distribution with a variance of 0.12. The *average delay* of  $T_{DHL}$  is 48.46 ns, and the standard deviation is 5.84 ns. To increase robustness against process variations and decrease the standard deviation, the dimensions of MN0–MN13, which are responsible for biasing the circuit, can be increased while maintaining the same aspect ratio “W/L”. But, a trade-off must be made between the chip area and the sensitivity of the generated deadtime to process variations. The operation of the proposed circuit is evaluated under different programming commands (i.e., 0FFF) and temperatures ( $-40$  °C to  $80$  °C). Fig. 7 (b) presents the simulated results. The value of  $T_{DHL} = 50$  ns is selected by the command “0FFF”, and varies from 42 to 52ns for the above temperature range.

#### D. Optimal Deadtime Mathematical Analysis

A simplified power converter circuit is illustrated in Fig. 8 to derive the equation of the optimum required deadtime for a buck converter. Fig. 8 (a) shows the converter circuit when the HSS is turned on and the LSS is turned off. The HSS and LSS are in their ‘off’ states within the deadtime duration. Meanwhile, Figs. 8 (b) and (c) show the operation at the beginning of the deadtime with the effective parasitic capacitance and the equivalent circuit of the converter during the deadtime operation with the charged equivalent capacitor in node  $V_{SW}$ , respectively. Within the deadtime duration, the HSS and LSS are turned off. In this condition, the total equivalent capacitance in node  $V_{SW}$  is given by

$$C_{eq} = C_{gd-LS} + C_{ds-LS} + C_{gs-HS} + C_{ds-HS} + C_{par}, \quad (2)$$

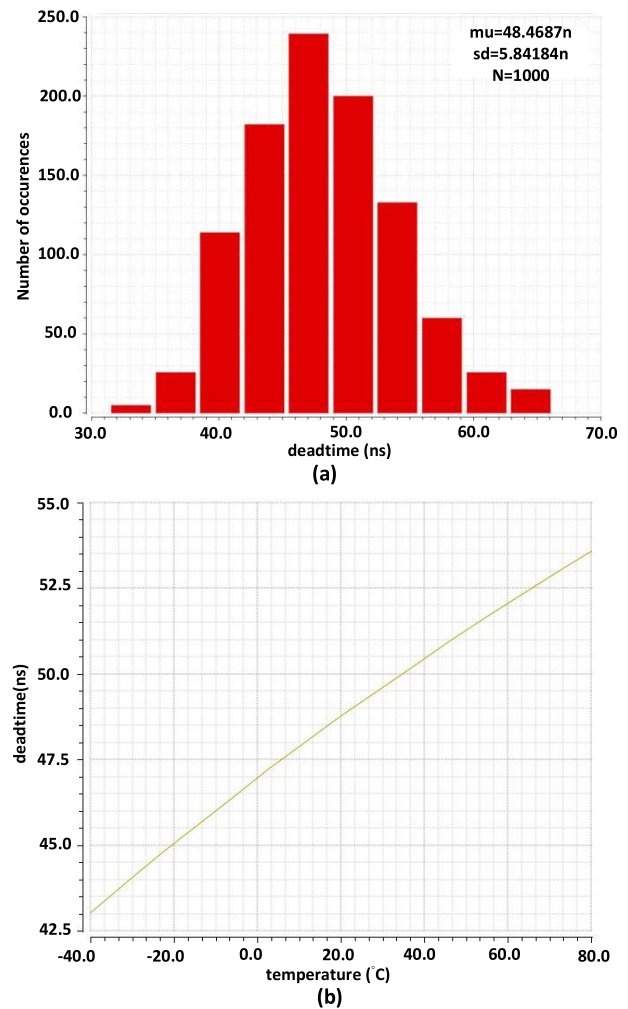


Fig. 7. (a) Evaluation of the proposed WRM-TDC operation with Monte-Carlo simulation, (b) assessment of a certain dead time value for different temperatures.

where  $C_{par}$  is the parasitic capacitance of the power switch packaging and wire-bonding. Fig. 1 (b) shows that the deadtimes  $T_{DLH}$  and  $T_{DHL}$  are set asymmetrically to ensure a secure operation against shoot-through and provide efficient conversion of the power converter. To increase the buck converter efficiency, the  $T_{DHL}$  must be set in its optimal state, which is when the charged  $C_{eq}$  is totally discharged ( $V_{Ceq}(T_{DHL}) = 0$ ), then the LSS must be activated. Otherwise, if  $T_{DHL}$  is set longer or shorter than the optimal time, the loss is increased, and the buck converter will not be efficiently designed. The optimal duration condition for  $T_{DLH}$  is determined to avoid shoot-through. The value of  $T_{DLH}$  can be reduced as long as shoot-through does not occur. The equivalent circuit of the buck converter is shown in Fig. 8(c)

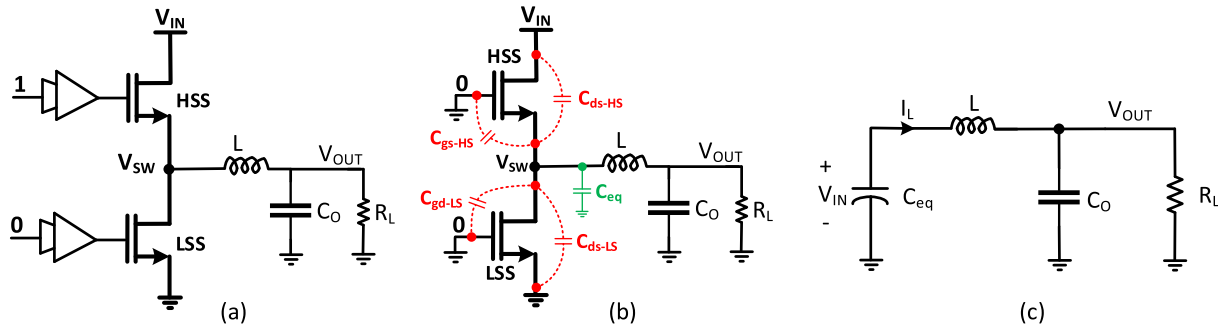


Fig. 8. Buck converter operation evaluation. (a) Simplified circuit while the HSS is turned on and the LSS is turned off, (b) operation in the beginning of deadtime with effective parasitic capacitance, and (c) equivalent circuit during deadtime operation with the charged equivalent capacitor in the node  $V_{SW}$ .

where  $C_{eq}$  is charged in advance by  $V_{IN}$  at the beginning of the deadtime. The analysis of the deadtime generation begins with:

$$V_L(t) = L \frac{dI_L(t)}{dt}, \quad (3)$$

which can be rearranged as follows when evaluated within a given time interval,  $\Delta T$ :

$$V_L \Delta T = L \Delta I_L, \quad (4)$$

where  $V_L$  equals to  $V_{IN} - V_{OUT}$ . In this buck converter,  $\Delta T$  is for the time duration of the HSS operation for one cycle of the input PWM, which is obtained by the product  $DT_s$ . Thus, in (4),  $\Delta T$  must be replaced by  $DT_s$  as follows:

$$(V_{IN} - V_{OUT}) DT_s = L \Delta I_L, \quad (5)$$

where  $D$  and  $T_s$  are the duty cycle and period of the input PWM, respectively. In the buck converter,  $D$  is equal to  $V_{OUT}/V_{IN}$ [46]. The value of  $\Delta I_L$  is evaluated by substituting the  $V_{OUT}/V_{IN}$  instead of  $D$  in (5) as follows:

$$\begin{aligned} \Delta I_L &= \frac{(V_{IN} - V_{OUT}) \left( \frac{V_{OUT}}{V_{IN}} \right) \frac{1}{f_s}}{L} \\ &= \frac{V_{OUT} (V_{IN} - V_{OUT})}{2LV_{IN}f_s}. \end{aligned} \quad (6)$$

In Fig. 1(b), the red curve shows the currents flowing into the circuit during the deadtime, in which  $I_{L(peak)}$  is equal to  $I_{Load} + (\Delta I_L/2)$ . According to (6),  $I_{L(peak)}$  can be defined by:

$$I_{L(peak)} = I_{load} + \frac{\Delta I_L}{2} = I_{load} + \frac{V_{OUT} (V_{IN} - V_{OUT})}{2LV_{IN}f_s}. \quad (7)$$

After setting an optimal deadtime for the buck converter, the zero-voltage switching condition would occur [51]. In this condition, the available charge in the  $C_{eq}$  is discharged by converter's inductance before turning-on the LSS. According to the equation of the equivalent capacitance in node  $V_{SW}$  at a given time,

$$I_{Ceq} = C_{eq} \frac{dV_{Ceq}(t)}{dt} \Rightarrow I_{Ceq} = C_{eq} \frac{\Delta V_{Ceq}(t)}{\Delta t}. \quad (8)$$

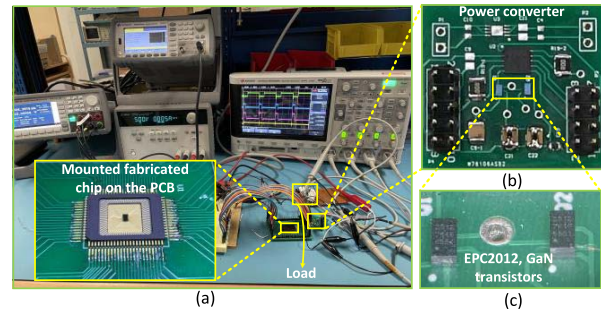


Fig. 9. Experimental setup: (a) equipment to measure the performance of fabricated WRM-TDC, (b) enlarged power converter, and (c) enlarged power GaN transistors of EPC2012.

During the discharge of the equivalent capacitance,  $I_{Ceq-discharge} = I_L$ . Hence,

$$\Delta t = \frac{C_{eq} \Delta V_{Ceq}(t)}{I_L}. \quad (9)$$

As shown in Fig. 1(b),  $I_L$  is approximately equal to  $I_{L(peak)}$  ( $I_L(t) \approx I_{L(peak)}(t)$ ) within the deadtime duration, and  $\Delta V_{Ceq}(t)$  is equal to  $V_{IN} - V_{Ceq}(T_{DHL}) = V_{IN} - 0 = V_{IN}$  in the optimal deadtime conditions ( $V_{Ceq}(T_{DHL}) = 0$ ). This condition holds for all  $\Delta t$  equal to  $T_{DHL}$ , specifically at its optimal value. From the equation of  $I_{L(peak)}$  in (7), the optimal deadtime is given by

$$\Delta t_{opt} = \frac{C_{eq} V_{IN}}{I_{L(peak)}} = \frac{C_{eq} V_{IN}}{I_{load} + \frac{V_{OUT}(V_{IN} - V_{OUT})}{2LV_{IN}f_s}} = T_{DHL}, \quad (10)$$

where  $I_{load} = V_{OUT}/R_L$ . The deadtime  $T_{DLH}$  must be minimized as much as possible to avoid shoot-through. An efficient buck converter design must address this requirement.

### III. MEASURED PERFORMANCE

#### A. Experimental Results of Proposed WRM-TDC

Fig. 9 shows the experimental test bench. The experimental results of the proposed WRM-TDC are measured by soldering it on a printed circuit board (PCB) in the laboratory. Two 16-bit flat ribbon cables are utilized to send the digital commands to the proposed circuit to program the different  $T_{DHL}$  and  $T_{DLH}$  at the circuit output. A pulse-shaped signal was generated with a function generator as input signal. The deadtimes  $T_{DHL}$  and



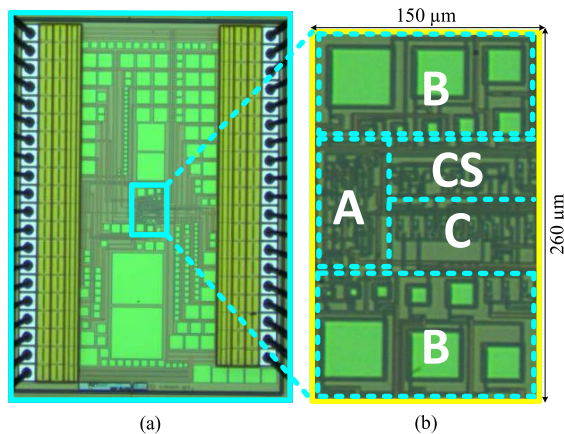


Fig. 10. Chip micrograph of the proposed WRM-TDC fabricated in  $0.35\ \mu\text{m}$  CMOS process (a) die micrograph, (b) enlarged core including different circuit parts of A, B, C, and CS.

$T_{DLH}$  are measured with an oscilloscope between the non-overlapping signals. Different capacitive loads of  $1\text{pF}$ - $10\text{nF}$  was used at each output of under test chip to measure the performance of fabricated chip.

The chip micrograph of the proposed WRM-TDC fabricated in  $0.35\ \mu\text{m}$  CMOS process is presented in Fig. 10. A wire-bonded die micrograph is presented in Fig. 10(a). The enlarged cores of the fabricated chip, which includes the different parts of A, B, C, and CS and occupies  $150\ \mu\text{m} \times 260\ \mu\text{m}$  of silicon area, are shown in Fig. 10(b). Fig. 11 shows the measured deadtimes generated by the WRM-TDC. The measured minimum and maximum selectable deadtimes corresponding to programming commands of 0000 and FFFF are presented in Fig. 11(a) and (b), respectively. A minimum deadtime of  $T_{DLH} = 9.2\ \text{ns}$  is measured for the proposed WRM-TDC, while the circuit was supplied with  $V_{DD} = 5.0\ \text{V}$ , and the operating frequency was  $f_s = 1\ \text{MHz}$ . A maximum deadtime of  $T_{DHL} = 1\ \mu\text{s}$  is measured, while the fabricated prototype was supplied with  $V_{DD} = 3.3\ \text{V}$ , and the operating frequency was  $f_s = 200\ \text{kHz}$ . In Fig. 11, the green waveform corresponds to the input pulse signal applied to the chip. The signals in blue and red correspond to the output of the chip, which can be used as appropriate driving signals for the HS and LS of the buck converters. The measured  $T_{DLH}$  and  $T_{DHL}$  are shown in blue and red in Fig. 12(a), respectively. The circuit is connected to  $V_{DD} = 5.0\ \text{V}$ , a capacitive load  $C_L = 1\text{pF}$  was used, and the operating frequency was set to  $f_s = 1\ \text{MHz}$ . The measured results are categorized based on the operation of the circuit in four different regions. In the first region, the proposed WRM-TDC is initialized to produce the shortest possible deadtime. In this configuration, parts A and B are enabled, and part C is disabled (MN0-MN13,  $T_{1a}$ ,  $T_{1b}$ ,  $T_{3a}$ , and  $T_{3b}$  are in the circuit, while the integrated capacitors are disabled). In this first region, the measured  $T_{DLH}$  and  $T_{DHL}$  are  $9.2$  and  $10.8\ \text{ns}$ , respectively. The circuit can be programmed to work in the other regions to increase the deadtime. In Region 2, part A is disabled step by step by received commands, part B is enabled, and part C is disabled. The LSB  $b_0$  is set to “1” to increase the delay whereas the other bits are kept at “0” (i.e., the command of “0001”, which is the hexadecimal code corresponding to the controlling switches status, is sent to the WRM-TDC). Two bits are dedicated to Region 2. In this part, the measured

deadtime resolution is  $0.2\ \text{ns}$  with  $1\%$  precision. Accordingly, the maximum achievable deadtimes for Region 2 are  $T_{DLH} = 9.6\ \text{ns}$  and  $T_{DHL} = 11.2\ \text{ns}$  under  $V_{DD} = 3.3\ \text{V}$  and  $f_s = 1\ \text{MHz}$ . The circuits of Region 3 are activated step by step by the commands to achieve longer deadtimes than what is attained in Region 2. In Region 3, parts A and C are disabled, and part B is enabled. The measured resolutions of the circuit in Region 3 for  $T_{DLH}$  and  $T_{DHL}$  are measured at approximately  $0.3$  and  $1\ \text{ns}$  (the difference between two measured deadtimes corresponds to two commands), respectively, while the number of bits dedicated to this region is 6 bits. Accordingly, the maximum measured  $T_{DLH}$  and  $T_{DHL}$  are  $12$  and  $16.6\ \text{ns}$ , respectively. Parts A and C are disabled, while part B is enabled by the commands to measure the results in Region 3. A longer deadtime can be achieved in Region 4 where the circuit is using a capacitive bank as delay element. In Region 4, eight different values of integrated capacitors (Table I) that correspond to eight controlling bits are embedded. The longest  $T_{DLH} = 250\ \text{ns}$  and  $T_{DHL} = 300\ \text{ns}$  are measured in Region 4 for commands of 01FF to FFFF. Parts A and B are disabled, and part C was enabled by the commands to measure the results in Region 4. The measured results in Fig. 12(b) show the performance of the circuit in various conditions. The circuit is configured by the different commands while it is connected to  $V_{DD} = 3.3\ \text{V}$ , the capacitive load was changed from  $C_L = 1\ \text{pF}$  to  $C_L = 12\ \text{pF}$ , and the operating frequency was set to  $f_s = 400\ \text{kHz}$ . In this condition, the measured  $T_{DLH}$  and  $T_{DHL}$  are  $11\ \text{ns}$  to  $450\ \text{ns}$  and  $16\ \text{ns}$  to  $1000\ \text{ns}$ , respectively, depending on the configuration, as shown in Fig. 12(b). The presented experimental results in Fig. 12 (b) demonstrate that the configured circuit can produce stable  $T_{DHL}$  and  $T_{DLH}$  for different capacitive loads at a fixed  $V_{dd}$ .

Fig. 13(a) shows that the measured power dissipation of the fabricated chip corresponds to all ranges of deadtime produced by the proposed WRM-TDC in the different programmed circuit configurations. The results are measured for five different values of capacitive loads. The largest power dissipation corresponds to the “0000” command (shortest delay) because all the tunable capacitive parts of A and B are added at the load in the circuit in this condition. The power dissipation results follow a descending curve (Fig. 13 (a)) due to the removability of the tunable parts of A and B by the commands of “0001” to “00FF”. The results follow an ascending curve due to inclusion of the integrated capacitors of part C at a longer deadtime. The circuit programmed with command “FFFF” is tested with  $C_L = 10\ \text{nF}$  at  $V_{dd} = 3.3\ \text{V}$  and  $f_s = 200\ \text{kHz}$  to see the performance of circuit in the case when driving big capacitive loads. The output waveforms of the chip are presented in Fig. 13(b). Fig. 13 shows that a long deadtime of  $T_{DHL} = 960\text{ns}$  with the command of “FFFF” is achieved while the circuit is driving two large capacitive loads at its outputs. For  $T_{DLH}$ , the value is set as short as possible, at the limit before shoot-through occurs. In Fig. 13(b), the red waveform (i.e. the LSS activation signal) reaches zero then the blue one (i.e. the HSS activation signal) starts to increase. Given that the waveforms have no overlap between the transition, consequently, shoot-through does not occur. In this condition, the proposed deadtime circuit consumed  $41\ \text{mW}$ , while the measured output signal slew rate (SR) was  $0.62\ \text{V/ns}$ . The circuit has two outputs, namely, LS and HS,

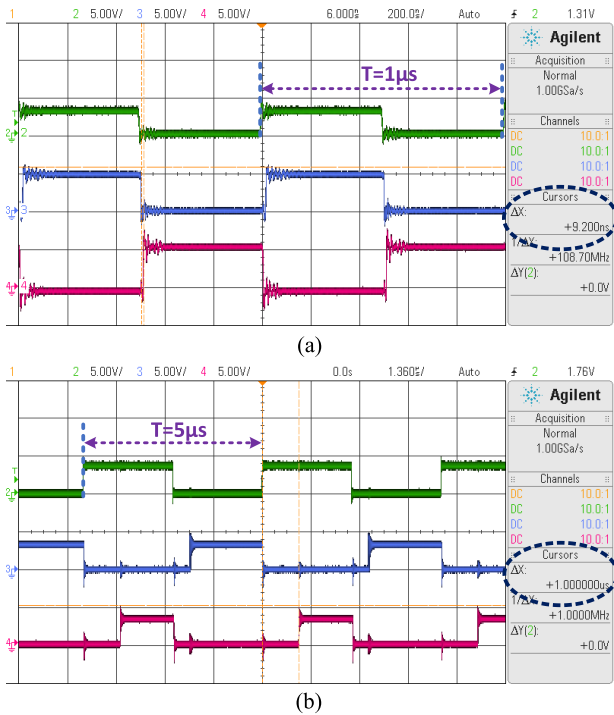


Fig. 11. Measured generated dead-times by WRM-TDC: (a) minimum produced dead-time of  $T_{DLH} = 9.2$  ns at  $C_L = 1$  pF,  $V_{dd} = 5.0$  V, and  $f_s = 1$  MHz; (b) maximum attained dead-time of  $T_{DHL} = 1$   $\mu$ s at  $C_L = 5$  pF,  $V_{dd} = 3.3$  V, and  $f_s = 200$  kHz.

where the dynamic current is consumed to drive the capacitive loads. Therefore, to calculate the slew rate of the waveform at each output, half of the consumed dynamic current can be divided by the capacitive load ( $SR = 0.5 \cdot i_{dynamic} / (C_L) = 0.5 \cdot 12.4$  mA/10 nF = 0.62 V/ns), which is reasonable for typical applications. Fig. 14 illustrates the measured power consumption versus operating frequency at different tuning commands,  $C_L = 10$  pF, and  $V_{DD} = 3.3$  V. According to the measured results, the power consumption increases with  $f_s$ . However, the maximum  $f_s$  is limited depending on the tuning commands. At FFFF, where the circuit can produce maximum  $T_{DLH}$  and  $T_{DHL}$ , the  $f_s$  is limited to 1 MHz. The circuit programmed with command 0000 to generate the minimum  $T_{DLH}$  and  $T_{DHL}$  can work properly up to 18 MHz, and the measured power consumption is presented in Fig. 14. The circuit programmed with command 0000 consumed approximately 21 mW at  $f_s = 18$  MHz, whereas it dissipated 0.48 mW for command FFFF at  $f_s = 200$  MHz.

### B. WRM-TDC Circuit Validation With a Buck Converter

To validate the operation of the proposed WRM-TDC, a buck converter is mounted on a PCB, as shown in Fig. 9. The fabricated chip is connected to the buck converter to measure the improvement of efficiency in the optimal  $T_{DHL}$  compared to a fixed  $T_{DHL}$ . Fig. 15 shows the optimized buck converter design waveforms with optimal  $T_{DHL}$  and minimum  $T_{DLH}$  values. The converter specifications are  $R_L = 80\Omega$ ,  $V_{IN} = 12$  V,  $V_{out} = 2.0$  V, duty cycle = 16.7%,  $I_{Load} = 25$  mA,  $f_s = 0.4$  MHz,  $T_{DLH} = 12$  ns, and  $T_{DHL} = 80$  ns. The conditions of  $t_{Df} = 0$ ,  $t_{Dr} = 0$ ,  $t_{tL} = 0$ , and  $t_{tL} = 0$  in the  $V_{SW}$  waveform are achieved for optimal  $T_{DHL}$  and minimum  $T_{DLH}$ . In other

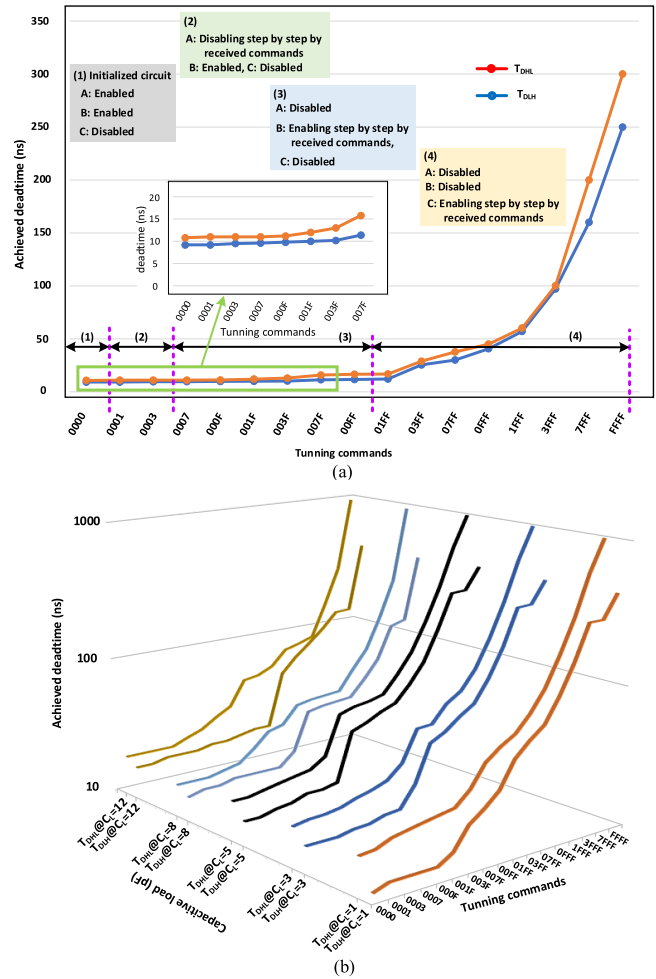


Fig. 12. Measured  $T_{DLH}$  and  $T_{DHL}$  from the fabricated chip in the various conditions: (a) different configurations of circuit at  $V_{dd} = 5.0$  V, capacitive load  $C_L = 1$  pF, and  $f_s = 1$  MHz; (b) different configurations of the circuit at  $V_{dd} = 3.3$  V, capacitive load  $C_L = 1$  pF to  $C_L = 12$  pF, and  $f_s = 400$  kHz.

words, the LSS Gate signal can increase exactly when the  $V_{SW}$  signal reaches zero ( $C_{eq}$  is fully discharged ( $V_{Ceq}(T_{DHL} = 0)$ ). Thus, compared with the use of a fixed random deadtime, the efficiency improves by 12%.

In order to set  $I_{load} = 25$ –400 mA (i.e. the inductor direct current resistance), the specifications of the buck converter are  $V_{IN} = 12$  V,  $f_s = 0.4$  MHz,  $V_{OUT} = 2$  V,  $L = 100$   $\mu$ H,  $C_O = 4.4$   $\mu$ F,  $DCR = 200$  m $\Omega$ ,  $ESR = 100$  m $\Omega$  (capacitor equivalent series resistance), and  $R_L = 80\Omega$ –5 $\Omega$ . Thus, we can attain maximum efficiency of the buck converter at different loads (25–400 mA). Fig. 16 (a) presents the measured results in three different conditions including 1)  $T_{DLH} = 12$  ns,  $T_{DHL} =$  optimum at different  $I_{load}$ , 2)  $T_{DLH} = T_{DHL} = 50$  ns (fixed deadtime determined by proposed circuit), and 3)  $T_{DLH} = T_{DHL} = 12$  ns (fixed deadtime). At  $f_s = 0.4$  MHz, the measured efficiency is changed from 53% (at  $I_{out} = 25$  mA and  $T_{DHL} = T_{DLH} = 12$  ns) to 80% (at  $I_{out} = 100$  mA and  $T_{DLH} = 12$  ns,  $T_{DHL} =$  optimum). The curves in Fig. 16 (a) are obtained using an array of resistive loads between 80 and 5.0  $\Omega$ . The resistive loads are connected to the output of the described buck converter and manually switched between each measurement from 80  $\Omega$  to 5.0  $\Omega$ . The buck converter is

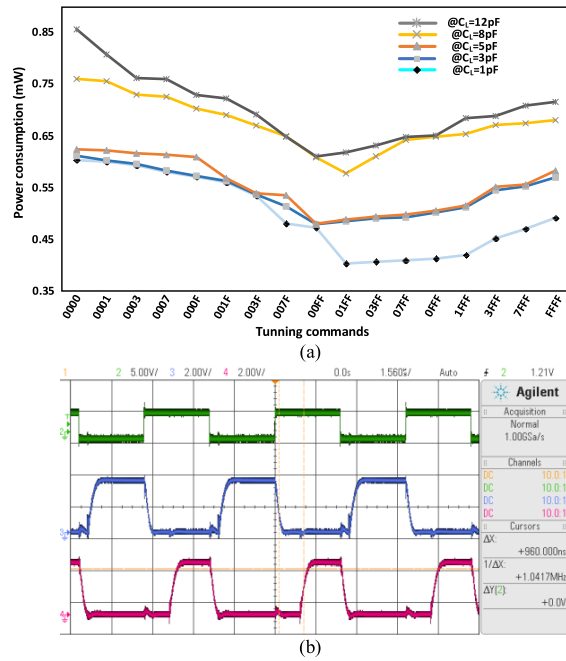


Fig. 13. (a) Measured power consumption versus tuning commands at different capacitive loads. (b) Measured waveforms of proposed circuit at  $V_{dd} = 3.3V$ ,  $f_s = 200kHz$ , and capacitive load of  $C_L = 10$  nF at each output of chip.

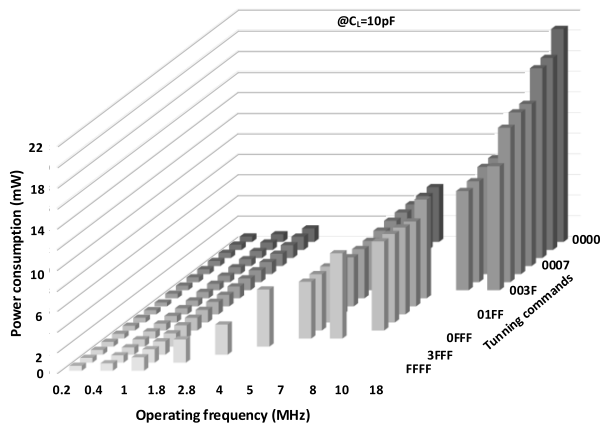


Fig. 14. Measured power consumption versus operating frequency at different tuning commands.

connected to a 12.0V power supply and the duty cycle of the input PWM is set to 16.66% [duty cycle =  $(V_O/V_{IN}) \times 100 = (2.0V/12.0V) \times 100 = 16.66\%$ ] by using a function generator. For each resistive load, the output and input power of the buck converter are measured, and the efficiency is then calculated. In addition, the three aforementioned deadtime scenarios are applied. Fig. 16 (a) shows the measured efficiencies versus  $I_{load}$  for these three deadtime scenarios. In Fig. 16(a), the red curve follows the maximum efficiency.

Fig 16 (a) shows that, although in the blue curve, the value of  $T_{DHL}$  is set to 12 ns (shorter than the optimal value in Fig 16 (b) for different loads), the achieved efficiency is lower than the others. Indeed, the efficiency of the buck converter with minimum  $T_{DLH}$  and optimal  $T_{DHL}$  at  $I_{load} = 25mA$  is improved by 12% compared to converter with fixed deadtime

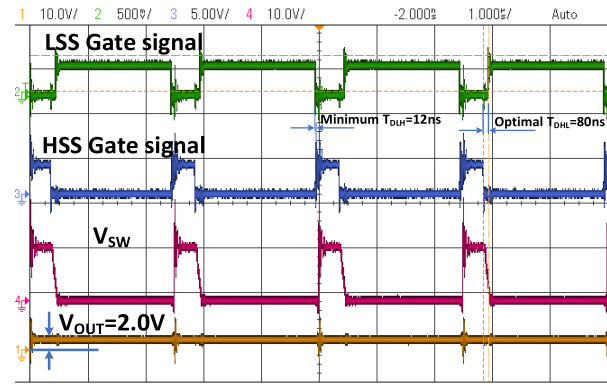


Fig. 15. Buck converter waveforms with optimal  $T_{DHL}$  and minimum  $T_{DLH}$  under efficient design.

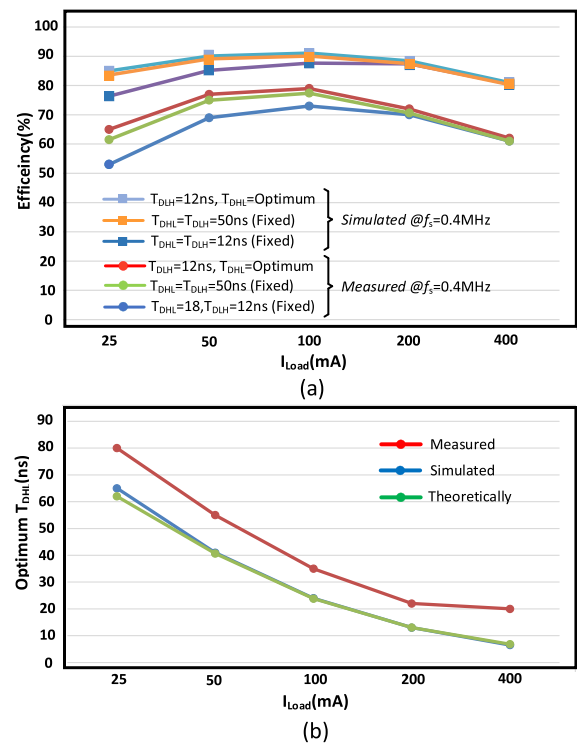


Fig. 16. Measured results (a) achieved efficiency of the implemented buck converter for different  $T_{DHL}$  and  $T_{DLH}$  at 0.4 MHz versus different  $I_{load}$ . (b) comparing the measured, simulated, and calculated optimal  $T_{DHL}$ .

of  $T_{DLH} = T_{DHL} = 12ns$ . In summary, a significant outcome of the analysis is that although the  $T_{DLH}$  must be as short as possible (before shoot through occurs) to attain maximum efficiency, it is different for  $T_{DHL}$ . In the buck converters at exact optimal  $T_{DHL}$  (no longer and no shorter than the optimal condition), the maximum efficiency would be achieved.

The efficiency of buck converter for  $I_{load} = 100$  mA improved by 7% due to the optimal  $T_{DHL}$ . The optimal  $T_{DHL}$  that corresponds to different  $I_{out}$  for frequency of 0.4 MHz are plotted in Fig. 16(b). These optimal  $T_{DHL}$ , which are attained based on the measured maximum efficiency at different  $I_{out}$ , are compared with the calculated  $T_{DHL}$  on the basis of (10) and with the simulated optimal  $T_{DHL}$  as well. The results presented in Fig. 16(b) confirm the accuracy of (10). Fig. 16 (b) shows that the maximum efficiency reached by the

TABLE II  
PERFORMANCE COMPARISON OF THE PROPOSED WRM-TDC WITH SIMILAR WORKS

References	TPEL'21, [42]	ECCE'20, [48]	ISSC'16, [49]	ESSCIRC'11, [54]	JSSC'16, [55]	This work
Technology(nm)	--	250	350	65	180	<b>350</b>
Results	Measured	Measured	Measured	Measured	Measured	<b>Measured</b>
Input Voltage(V)	Up to 40V	12	3-40	Up to 5	12-18	<b>6-24</b>
Output Current (mA)	240-8800	200-1000	10-1200	Up to 120	50-500	<b>25-400</b>
Tunning range (ns)	Up to 50	0.4-9.4	0.9-10.4	1-32	3-28	<b>9.2-1000</b>
Power Switches	GaN	GaN	GaN	Si MOS	Si MOS	<b>GaN</b>
Bootstrap Capacitor	On-chip	On-chip	On-chip	External	External	<b>External</b>
Maximum efficiency (%)	95.8@ $V_{IN}=30V$	87.9%	90.7@ $V_{IN}=12V$	76.4@ $V_{IN}=3V$	81.2@ $V_{IN}=12V$	<b>90@<math>V_{IN}=24V</math></b>
Efficiency improvement	1.9%@ $V_{IN}=40V$ , 4.5%@ $V_{IN}=30V$	4%@ $I_{OUT}=1A$	8.5%	3%	6%	<b>12%@<math>I_{OUT}=25mA</math>, 5.1%@<math>V_{IN}=24V</math></b>

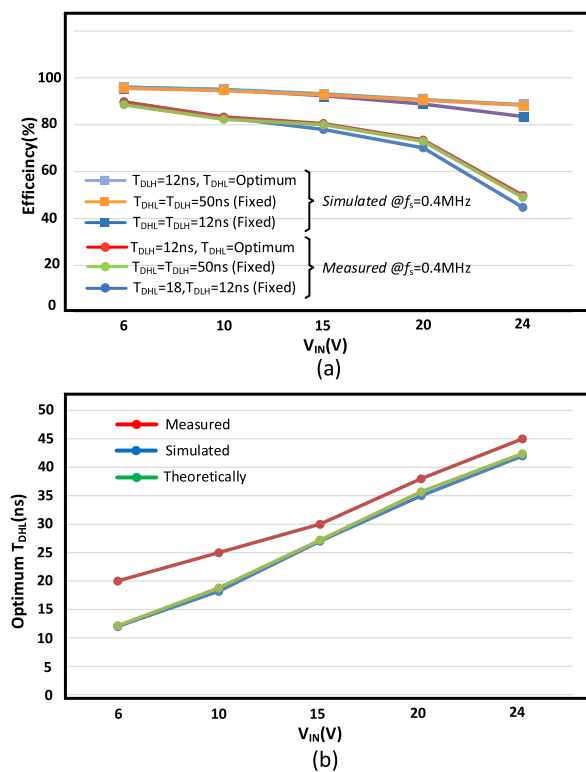


Fig. 17. Measured results (a) achieved efficiency of the implemented buck converter for different  $T_{DHL}$  and  $T_{DLH}$  at 0.4 MHz versus different  $V_{IN}$ , (b) comparing the measured, simulated, and calculated optimal  $T_{DHL}$ .

simulated converter at  $f_s = 0.4$  MHz for  $I_{load} = 25\text{-}400$  mA is achieved with the optimal deadtimes of 65–6.5 ns.

A buck converter with the following specifications is used to validate the anticipated dependency of  $T_{DHL}$  over  $V_{IN}$  in (10):  $V_{OUT} = 3.3$  V,  $f_s = 0.4$  MHz,  $L = 100$   $\mu$ H,  $C_O = 4.4$   $\mu$ F, DCR = 200 m $\Omega$  (inductor direct current resistance), ESR = 100 m $\Omega$  (capacitor equivalent series resistance),  $R_L = 33$   $\Omega$  ( $I_{out} = V_{OUT}/R_L = 100$  mA), and  $V_{IN}$  varied from 6.0 V to 24.0 V. The maximum efficiency of the buck converter for different  $V_{IN}$  (6.0–24.0 V) is attained. Fig. 17 (a) presents the measured results of the converter in three different conditions, 1)  $T_{DLH} = 12$  ns,  $T_{DHL} = \text{optimum}$  at different  $V_{IN}$ , 2)  $T_{DLH} = T_{DHL} = 50$  ns (fixed deadtime), and 3)  $T_{DLH} = T_{DHL} = 12$  ns (fixed deadtime). The results are shown in Fig. 17(a). The efficiency changes from 44.1% (at

$V_{IN} = 24$  V,  $T_{DLH} = 12$  ns, and  $T_{DHL} = 18$  ns) to 90% (at  $V_{IN} = 6.0$  V,  $T_{DLH} = 12$  ns,  $T_{DHL} = \text{optimum}$ ). The presented curves in Fig. 17 (a) are obtained by setting the resistive load to 33  $\Omega$ . The buck converter is connected to the power supply of 6.0V and the duty cycle of the input PWM is set to 33.33% [duty cycle =  $(V_O/V_{IN}) \times 100 = (2.0V/6.0V) \times 100 = 33.33\%$ ] by using a function generator. This setup is implemented for different  $V_{IN}$  from 6.0V to 24.0V and the duty cycle is set manually in each step. For each  $V_{IN}$ , the output and input power of the buck converter are measured and the efficiency is then calculated. In addition, the three aforementioned deadtime scenarios are applied. Fig. 17 (a) shows the measured efficiencies versus  $V_{IN}$  for these three deadtime scenarios. The efficiency of the converter with optimal deadtime for  $V_{IN} = 24$  V is improved by 5.1% compared with the efficiency measured with a fixed deadtime (at  $V_{IN} = 6.0$  V and  $T_{DLH} = T_{DHL} = 12$  ns). The improvement of efficiency for  $V_{IN} = 6.0$  V is of 0.4% due to the optimal  $T_{DHL}$  compared with the fixed  $T_{DHL}$ . In Fig. 17(b), the optimal  $T_{DHL}$  that corresponds to different  $V_{IN}$  is presented. These optimal  $T_{DHL}$ , which are attained based on the measured maximum efficiency at different  $V_{IN}$ , are compared with the calculated  $T_{DHL}$  based on (10) and with the simulated optimal  $T_{DHL}$  as well. The presented results in Fig. 17 (b) confirm the accuracy of (10). The maximum efficiency achieved for the simulated converter at  $f_s = 0.4$  MHz for  $V_{IN} = 6.0\text{-}24$  V with the optimal deadtimes of 12-42 ns is shown in Fig. 17(a).

#### IV. DISCUSSION AND PERFORMANCE COMPARISON

Table II compares the performance of the presented WRM-TDC with other solutions. A deadtime optimization technique based on mathematical analysis is introduced in [42]. As shown in Table II, the optimized deadtime circuit increases the efficiency by 4.5% compared to the fixed deadtime. One disadvantage of the approach described in [42] is that the values of both  $T_{DLH}$  and  $T_{DHL}$  must be changed based on the circuit parameters. However, we demonstrated that the value of  $T_{DLH}$  must be minimized while only the value of  $T_{DHL}$  should be determined using the derived equations. According to the measured results, the efficiency can be improved by up to 12% when using the proposed circuit and deadtime optimization method. A bang-bang deadtime circuit that can generate a deadtime ranging from 0.4 ns to 9.4 ns is presented in [48]. The circuit proposed in [48] is suitable for applications with low  $V_{IN}$  and high  $I_{out}$  requiring a short deadtime. The work presented in [49] can improve

efficiency by 8.5%. However, the range of generated deadtime is restricted between 0.9 ns to 10.4 ns, which cannot support a wide range of power converter applications. The solutions presented in [54] and [55] lead to maximum efficiencies of 76.4% and 81.2%, respectively, while the efficiency improvement is between 3%-6%. In Table II, the proposed circuit achieves the wider tuning deadtime range, producing delays between 9.2 ns and 1000 ns. Additionally, the proposed optimization technique improves the efficiency by up to 12% compared to a fixed deadtime. Another advantage of the proposed circuit is to accommodate buck converters with a wide range of  $I_{OUT}$  and  $V_{IN}$ . In DC-DC converters, the three main types of losses are: 1-switching, 2-conduction, and 3-deadtime. Our method aims to minimize the deadtime loss. Switching and deadtime losses are dominant for light loads and high  $V_{IN}$  but conduction loss is dominant for heavy loads. Accordingly, given that our proposed circuit improves deadtime and switching losses, Figs. 16 (a) and 17 (a) show greater efficiency improvement in light loads and high  $V_{IN}$ .

## V. CONCLUSION

We proposed a reconfigurable deadtime circuit to produce a vast range of delays between the high and low side waveforms activating a power converter. Three reconfigurable parts are allocated for the designed circuit to have a variable deadtime to accommodate different types of power converter loads and input voltage. In addition, the tunable procedure can help in finding an optimal deadtime for a given power converter to minimize deadtime loss, especially for GaN-based converters that suffer from the deadtime loss. The advantages of the proposed circuit include utilizing a digital approach to adjust the deadtime rely on three different adjustable topologies with different performance in the case of resolution. The circuit yields deadtimes ranging between 9.2 ns and 1000 ns, which a wide variety of power converters driving different loads and operating at various input voltages. According to the measured results, the fabricated chip dissipated 41 mW when configured to produce a long deadtime of 940 ns, while driving  $C_L = 10$  nF with a slew rate of 0.62 V/ns. The circuit operates up to 18 MHz when configured to generate the shortest deadtime of 9.2 ns. The fabricated chip was connected to a buck converter to validate the operation of the proposed circuit. The efficiency of the buck converter with minimum  $T_{DLH}$  and optimal  $T_{DHL}$  at  $V_{IN} = 24V$  is improved by 5.1% compared to when the converter is using fixed deadtimes of  $T_{DLH} = T_{DHL} = 12ns$ .

## APPENDIX

The power losses of a typical power converter shown in Fig. 1(a) using GaN power switches can be summarized in Table III. The  $P_{SW}$ ,  $P_{CON}$ ,  $P_{DT}$ ,  $P_{CAP}$ ,  $P_G$ ,  $P_{DCR}$ , and  $P_{ESR}$  are switching loss, conduction loss, dead-time loss, output capacitance loss, gate charge loss, DC resistance of the output inductance loss, and output capacitance ESR loss, respectively. These power converter losses can be categorized into two families. Time-dependent losses are those related to the converter's operating frequency ( $P_{SW}$ ,  $P_{DT}$ ,  $P_{CAP}$ , and  $P_G$ ). Time-independent losses (TIL) are due to physical specifications of the power switches and packaging specifications

TABLE III  
GaN POWER LOSS FORMULAS

Loss	Equation
$P_{SW}$	$P_{SW} = V_{IN} \times I_{OUT} \times f_{SW} \times (t_r + t_f)$
$P_{CON}$	$P_{CON} = R_{ON} \times I_{RMS}^2$
$P_{DT}$	$P_{DT} = f_s \times V_{SD} \times I_{OUT} \times (T_{DLH} + T_{DHL})$
$P_{CAP}$	$P_{CAP} = V_{IN} \times Q_{OSS} \times f_{SW}$
$P_G$	$P_G = (Q_{g-H} + Q_{g-L}) \times V_{gs} \times f_{SW}$
$P_{DCR}$	$P_{DCR} = (I_{OUT}^2 \times (\Delta I)^2 / 12) \times R_{DCR}$
$P_{ESR}$	$P_{ESR} = (\Delta I)^2 / 12 \times R_{ESR}$

( $P_{CON}$ ,  $P_{DCR}$ , and  $P_{ESR}$ ). One of the considerable TIL is due to the layout routing and bonding wires, which can account for approximately 24% of the total loss in a typical power converter [21]. In the  $P_{CON}$  equation, the  $I_{RMS}$  is calculated by

$$I_{RMS} = \sqrt{(I_{OUT}^2 + (\Delta I)^2 / 12)} D, \quad (11)$$

where  $D$  is the on-state percentage of either the HSS or the LSS in one cycle of power converter operation.

## ACKNOWLEDGMENT

The authors would like to thank Natural Sciences and Engineering Research Council of Canada, the Mathematics of Information Technology and Complex Systems (MITACS), CMC Microsystems, and the Canada Research Chair in Smart Biomedical Microsystems for providing the design and testing tools.

## REFERENCES

- [1] K. Onizuka, K. Inagaki, H. Kawaguchi, M. Takamiya, and T. Sakurai, "Stacked-chip implementation of on-chip buck converter for distributed power supply system in SiPs," *IEEE J. Solid-State Circuits*, vol. 42, no. 11, pp. 2404–2410, Nov. 2007.
- [2] W. Shin, M. Kim, S. Park, and N. Baek, "A real-time video processing implementation with massively parallel computation support," in *Proc. Int. Conf. Electron., Inf., Commun. (ICEIC)*, Jan. 2020, pp. 1–2.
- [3] A. Matamura *et al.*, "An 82-mW  $\Delta\Sigma$ -based filter-less class-D headphone amplifier with  $-93$ -dB THD+N, 113-dB SNR, and 93% efficiency," *IEEE J. Solid-State Circuits*, vol. 56, no. 12, pp. 3573–3582, Dec. 2021, doi: [10.1109/JSSC.2021.3100548](https://doi.org/10.1109/JSSC.2021.3100548).
- [4] K. Abdelfattah *et al.*, "A 40 nm fully integrated 82 mW stereo headphone module for mobile applications," *IEEE J. Solid-State Circuits*, vol. 49, no. 8, pp. 1702–1714, Aug. 2014.
- [5] A. Zakerian, S. Vaez-Zadeh, and A. Babaki, "A dynamic WPT system with high efficiency and high power factor for electric vehicles," *IEEE Trans. Power Electron.*, vol. 35, no. 7, pp. 6732–6740, Jul. 2020.
- [6] M. Karimi, H. Jouaicha, F. Lellouche, P.-A. Bouchard, M. Sawan, and B. Gosselin, "A 6.78-MHz robust WPT system with inductive link bandwidth extended for cm-sized implantable medical devices," in *Proc. 42nd Annu. Int. Conf. IEEE Eng. Med. Biol. Soc. (EMBC)*, Jul. 2020, pp. 4196–4199.
- [7] C.-T. Hsu, Y.-H. Chang, J.-S. Chen, H.-H. Lin, and J.-Y. Chou, "Implementation of IoT device on public fitness equipment for health physical fitness improvement," in *Proc. Int. Conf. Math. Comput. Sci. Eng. (MACISE)*, Jan. 2020, pp. 236–239.
- [8] Y.-C. Chu *et al.*, "On-chip AC-DC multiple-power-supplies module for transcutaneously powered wearable medical devices," *IEEE Trans. Ind. Appl.*, vol. 54, no. 2, pp. 1724–1736, Apr. 2018.
- [9] N. Tang, W. Hong, B. Nguyen, Z. Zhou, J.-H. Kim, and D. Heo, "Fully integrated switched-inductor-capacitor voltage regulator with 0.82-A/mm<sup>2</sup> peak current density and 78% peak power efficiency," *IEEE J. Solid-State Circuits*, vol. 56, no. 6, pp. 1805–1815, Jun. 2021.

- [10] Y. Jiang, M.-K. Law, Z. Chen, P.-I. Mak, and R. P. Martins, "Algebraic series-parallel-based switched-capacitor DC-DC boost converter with wide input voltage range and enhanced power density," *IEEE J. Solid-State Circuits*, vol. 54, no. 11, pp. 3118–3134, Nov. 2019.
- [11] M. Karimi, M. Ali, A. Hassan, M. Sawan, and B. Gosselin, "An active dead-time control circuit with timing elements for a 45-V input 1-MHz half-bridge converter," *IEEE Trans. Circuits Syst. I, Reg. Papers*, vol. 69, no. 1, pp. 30–41, Jan. 2022.
- [12] E. K. Sato, M. Kinoshita, Y. Yamamoto, and T. Amboh, "Redundant high-density high-efficiency double-conversion uninterruptible power system," *IEEE Trans. Ind. Appl.*, vol. 46, no. 4, pp. 1525–1533, Jul./Aug. 2010.
- [13] A. K. Sadigh, V. Dargahi, and K. A. Corzine, "Investigation of conduction and switching power losses in modified stacked multicell converters," *IEEE Trans. Ind. Electron.*, vol. 63, no. 12, pp. 7780–7791, Dec. 2016.
- [14] M. C. Caponet, F. Profumo, and A. Tenconi, "Evaluation of power losses in power electronic converters for industrial applications: Comparison among hard switching, ZVS and ZVS-ZCS converters," in *Proc. Power Convers. Conf.-Osaka*, Apr. 2002, pp. 1073–1077.
- [15] E. S. Glitz and M. Ordóñez, "MOSFET power loss estimation in LLC resonant converters: Time interval analysis," *IEEE Trans. Power Electron.*, vol. 34, no. 12, pp. 11964–11980, Dec. 2019.
- [16] F. Gamand, M. D. Li, and C. Gaquiere, "A 10-MHz GaN HEMT DC/DC boost converter for power amplifier applications," *IEEE Trans. Circuits Syst. II, Exp. Briefs*, vol. 59, no. 11, pp. 776–779, Nov. 2012.
- [17] K. Norling, C. Lindholm, and D. Draxelmayer, "An optimized driver for SiC JFET-based switches enabling converter operation with more than 99% efficiency," *IEEE J. Solid-State Circuits*, vol. 47, no. 12, pp. 3095–3104, Dec. 2012.
- [18] C. Yao *et al.*, "Adaptive constant power control of MHz GaN-based AC/DC converters for low power applications," *IEEE Trans. Ind. Appl.*, vol. 54, no. 3, pp. 2525–2533, May/June. 2018.
- [19] E. Velander *et al.*, "An ultralow loss inductor less  $dv/dt$  filter concept for medium-power voltage source motor drive converters with SiC devices," *IEEE Trans. Power Electron.*, vol. 33, no. 7, pp. 6072–6081, Jul. 2018.
- [20] G. Zulauf, S. Park, W. Liang, K. N. Surakitbovorn, and J. Rivas-Davila, "COSS losses in 600 V GaN power semiconductors in soft-switched, high- and very-high-frequency power converters," *IEEE Trans. Power Electron.*, vol. 33, no. 12, pp. 10748–10763, Dec. 2018.
- [21] H. Cao *et al.*, "A 12-level series-capacitor 48–1 V DC-DC converter with on-chip switch and GaN hybrid power conversion," *IEEE J. Solid-State Circuits*, vol. 56, no. 12, pp. 3628–3638, Dec. 2021, doi: 10.1109/JSSC.2021.3104328.
- [22] B. Sun, "Does GaN have a body diode?—Understanding the third quadrant operation of GaN," Texas Instrum., Dallas, TX, USA, Tech. Rep. SNOAA36, Feb. 2019.
- [23] S. Chellappan, "Design considerations of GaN devices for improving power converter efficiency and density," Texas Instrum., Dallas, TX, USA, Tech. Rep. SLYY124, Nov. 2017.
- [24] N. Mehta, "GaN FET module performance advantage over silicon," Texas Instrum., Dallas, TX, USA, Tech. Rep. SLYY071, Mar. 2015.
- [25] Y. Zhang and F. Yang, "Maximizing the performance of GaN with ideal diode mode," Texas Instrum., Dallas, TX, USA, Tech. Rep. SNOA932, Oct. 2020.
- [26] D. Jauregui, B. Wang, and R. Chen, "Power loss calculation with common source inductance consideration for synchronous buck converters," Texas Instrum., Dallas, TX, USA, Tech. Rep. SLPA009A, Jul. 2011.
- [27] J. Reinert, A. Brockmeyer, and R. W. De Doncker, "Calculation of losses in ferro- and ferrimagnetic materials based on the modified Steinmetz equation," *IEEE Trans. Ind. Appl.*, vol. 37, no. 4, pp. 1055–1061, Jul./Aug. 2001.
- [28] J. Li, T. Abdallah, and C. R. Sullivan, "Improved calculation of core loss with nonsinusoidal waveforms," in *Proc. 36th IEEE Ind. Appl. Conf. Rec. Annu. Meeting (IAS)*, vol. 4, Sep. 2001, pp. 2203–2210.
- [29] S. Rai, "GaN, SiC or Silicon Mosfet—A comparison based on power loss calculations," in *Proc. PCIM Asia Int. Exhib. Conf. Power Electron., Intell. Motion, Renew. Energy Energy Manage.*, Nov. 2020, pp. 1–9.
- [30] C. Yao, Y. Zhang, X. Zhang, H. Li, H. Chen, and J. Wang, "Adaptive constant power control and power loss analysis of a MHz GaN-based AC/DC converter for low power applications," in *Proc. IEEE Appl. Power Electron. Conf. Expo. (APEC)*, Mar. 2017, pp. 1755–1762.
- [31] B. Kim, S. Kim, D.-Y. Huh, J.-H. Choi, and M. Kim, "Hybrid resonant half-bridge DC/DC converter with wide input voltage range," in *Proc. IEEE Appl. Power Electron. Conf. Expo. (APEC)*, San Antonio, TX, USA, Mar. 2018, pp. 1876–1881.
- [32] Z. Zhang, O. C. Thomsen, and M. A. E. Andersen, "Soft-switched dual-input DC-DC converter combining a boost-half-bridge cell and a voltage-fed full-bridge cell," *IEEE Trans. Power Electron.*, vol. 28, no. 11, pp. 4897–4902, Nov. 2013.
- [33] D. Marx, P. Magne, B. Nahid-Mobarakeh, S. Pierfederici, and B. Davat, "Large signal stability analysis tools in DC power systems with constant power loads and variable power loads—A review," *IEEE Trans. Power Electron.*, vol. 27, no. 4, pp. 1773–1787, Apr. 2012.
- [34] M. Aghaei, R. Ayoubi, and S. Kaboli, "A high voltage variable inductor LCC resonant converter with high power factor over wide load range," in *Proc. 10th Int. Power Electron., Drive Syst. Technol. Conf. (PEDSTC)*, Shiraz, Iran, Feb. 2019, pp. 279–284.
- [35] M. Karimi *et al.*, "A 1.99-ns 0.5-pJ wide frequency range level shifter with closed-loop negative feedback," in *Proc. 18th IEEE Int. New Circuits Syst. Conf. (NEWCAS)*, Montreal, QC, Canada, Jun. 2020, pp. 174–177.
- [36] N. Ly, N. Aimaier, A. H. Alameh, Y. Blaquiere, G. Cowan, and N. G. Constantin, "A high voltage multi-purpose on-the-fly reconfigurable half-bridge gate driver for GaN HEMTs in 0.18- $\mu$ m HV SOI CMOS technology," in *Proc. 18th IEEE Int. New Circuits Syst. Conf. (NEWCAS)*, Montreal, QC, Canada, Jun. 2020, pp. 178–181.
- [37] Texas Instruments. 200V, 1.5A/3A Half Bridge MOSFET and GaN FET Driver With Adjustable Dead-Time, Datasheet. Accessed: Jan. 2019. [Online]. Available: <http://www.ti.com/product/LMG1210>
- [38] M. Karimi, M. Ali, A. Hassan, M. Sawan, and B. Gosselin, "A reconfigurable single-supply multiple-level down-shifter for system-on-chip applications," in *Proc. IEEE Int. Symp. Circuits Syst. (ISCAS)*, May 2021, pp. 1–5.
- [39] M. Amer *et al.*, "Fully integrated dual-channel gate driver and area efficient PID compensator for surge tolerant power sensor interface," in *Proc. 18th IEEE Int. New Circuits Syst. Conf. (NEWCAS)*, Montreal, QC, Canada, Jun. 2020, pp. 166–169.
- [40] M. Karimi *et al.*, "A versatile non-overlapping signal generator for efficient power-converters operation," in *Proc. IEEE Int. Symp. Circuits Syst. (ISCAS)*, Seville, Spain, Oct. 2020, pp. 1–5.
- [41] Y. Liang, "Intelligent automotive isolated gate driver with adaptive fault management and built-in switched mode power supply," in *Proc. IEEE Appl. Power Electron. Conf. Expo. (APEC)*, New Orleans, LA, USA, Mar. 2020, pp. 2643–2646.
- [42] M. Asad, A. K. Singha, and R. M. S. Rao, "Dead time optimization in a GaN-based buck converter," *IEEE Trans. Power Electron.*, vol. 37, no. 3, pp. 2830–2844, Mar. 2022.
- [43] M. Faizollah, M. Karimi, and A. M. Sodagar, "A low-power, generic biostimulator with arbitrary pulse shape, based on a central control core," *IEICE Electron. Exp.*, vol. 30, no. 7, pp. 3964–3975, Jul. 2015.
- [44] M. Karimi, M. Ali, A. Hassan, M. Sawan, and B. Gosselin, "A wide-range reconfigurable deadtime and delay element for optimal-power conversion," in *Proc. 19th IEEE Int. New Circuits Syst. Conf. (NEWCAS)*, Jun. 2021, pp. 1–4.
- [45] L. Schirone, M. Macellari, and F. Pellitteri, "Predictive dead time controller for GaN-based boost converters," *IET Power Electron.*, vol. 10, no. 4, pp. 421–428, Mar. 2017.
- [46] Y. Zheng, J. Guo, and K. N. Leung, "A single-inductor multiple-output buck/boost DC-DC converter with duty-cycle and control-current predictor," *IEEE Trans. Power Electron.*, vol. 35, no. 11, pp. 12022–12039, Nov. 2020.
- [47] P. K. Chiu, P. Y. Wang, S. T. Li, C. J. Chen, and Y. T. Chen, "A GaN driver IC with novel highly digitally adaptive dead-time control for synchronous rectifier buck converter," in *Proc. IEEE Energy Convers. Congr. Expo. (ECCE)*, Oct. 2020, pp. 3788–3792.
- [48] P. Y. Wang, P. K. Chiu, S. T. Li, C. J. Chen, and C. C. Hsu, "A 10 MHz GaN driver IC with bang-bang deadtime control for synchronous rectifier buck converter," in *Proc. IEEE Energy Convers. Congr. Expo. (ECCE)*, Oct. 2020, pp. 3776–3781.
- [49] X. Ke, J. Sankman, M. K. Song, P. Forghani, and D. B. Ma, "A 3-to-40 V 10-to-30 MHz automotive-use GaN driver with active BST balancing and  $V_{GS}$  dual-edge dead-time modulation achieving 8.3% efficiency improvement and 3.4 ns constant propagation delay," in *IEEE Int. Solid-State Circuits Conf. (ISSCC) Dig. Tech. Papers*, Jan. 2016, pp. 302–304.
- [50] S. Tang, J. Xi, and L. He, "A GaN-based MHz active clamp flyback converter with adaptive dual edge dead time modulation for AC-DC adapters," in *Proc. 43rd Annu. Conf. IEEE Ind. Electron. Soc. (IECON)*, Oct. 2017, pp. 546–553.

- [51] D. Gu, J. Xi, and L. He, "Digitally controlled GaN-based MHz active clamp flyback converter with dynamic dead time optimisation for AC-DC adapter," *IET Power Electron.*, vol. 13, no. 16, pp. 3777–3786, Dec. 2020.
- [52] M. Ekhtiari, T. Andersen, M. A. E. Andersen, and Z. Zhang, "Dynamic optimum dead time in piezoelectric transformer-based switch-mode power supplies," *IEEE Trans. Power Electron.*, vol. 32, no. 1, pp. 783–793, Jan. 2017.
- [53] Z. Lei, L. Haoyu, Y. Yu, and Y. Wang, "Optimum dead-time control method of phase-shifted converter to extend the ZVS range," in *Proc. IEEE Int. Telecommun. Energy Conf. (INTELEC)*, Oct. 2015, pp. 1–4.
- [54] G. Maderbacher, T. Jackum, W. Pribyl, M. Wassermann, A. Petschar, and C. Sandner, "Automatic dead time optimization in a high frequency DC-DC buck converter in 65 nm CMOS," in *Proc. (ESSCIRC)*, Sep. 2011, pp. 1919–1922.
- [55] J. Wittmann, A. Barner, T. Rosahl, and B. Wicht, "An 18 V input 10 MHz buck converter with 125 ps mixed-signal dead time control," *IEEE J. Solid-State Circuits*, vol. 51, no. 7, pp. 1705–1715, Jul. 2016.



**Mousa Karimi** (Member, IEEE) received the B.Sc. degree in electrical engineering from Azad University, Boushehr Branch, Iran, in 2009, and the M.Sc. degree from the K. N. Toosi University of Technology, Tehran, Iran, in 2012. He is currently pursuing the Ph.D. degree in microelectronics with Laval University, Quebec City, QC, Canada. His research interests include implantable microsystems, analog/digital/mixed-mode integrated circuits, wireless neural interfacing, and efficient-power converter design. Since the start of his Ph.D. program, he has

won several awards, including Mitacs Scholarship for collaboration with Thales-MITACS-NSERC/CRD, end of doctoral studies; and ReSMiQ Post-graduate Awards. The results of his research are presented in IEEE BioCAS, ISCAS, EMBC, and NEWCAS conferences. He is an Active Reviewer for many IEEE conferences, including the BioCAS, ISCAS, NEWCS, and EMBC conferences. He is a Reviewer of the IEEE TRANSACTIONS ON CIRCUITS AND SYSTEMS—I: REGULAR PAPERS.



**Mohamed Ali** (Member, IEEE) received the B.Sc. degree in electronics from the Faculty of Electronics Engineering, Menoufia University, Egypt, in 2005, the M.Sc. degree in electronics and communication engineering from Ain Shams University, Egypt, in 2011, and the joint Ph.D. degree in electronics and communication engineering from Ain Shams University and Polytechnique Montréal, Montreal, QC, Canada, in 2017. He was with Polytechnique Montréal as a Research Intern from 2015 to 2017 as a part of his Ph.D. Program. Since 2007, he has

been with the Microelectronics Department, Electronics Research Institute, Cairo, Egypt. He is a Post-Doctoral Fellow with the Department of Electrical Engineering, Polytechnique Montréal. His current research interests include analog, RF, mixed-signal design, systems-on-chip, and power management implementations.



**Amir Aghajani** received the B.Sc. degree in electrical engineering from the Sharif University of Technology, Tehran, Iran, in 2017, and the M.Sc. degree in microelectronic circuits from the University of Tehran, Tehran, in 2020. He is currently pursuing the Ph.D. degree in electrical engineering with the Biomedical Microsystems Laboratory, Laval University, Quebec City, QC, Canada. His main research interests include mixed-signal/analog IC design, power management circuits, DC-DC converters, wireless power transmission, and energy harvesting applications.



**Ahmad Hassan** (Member, IEEE) received the Ph.D. degree in electrical engineering from Polytechnique Montréal, QC, Canada, in 2019. He is currently a Post-Doctoral Researcher with the Polystim Neurotechnologies Laboratory, École Polytechnique de Montréal, Montreal, QC, Canada. His research is oriented toward high temperature microelectronics, including design and implementation of wireless power and data transmission systems dedicated for harsh environment applications.



**Mohamad Sawan** (Fellow, IEEE) received the Ph.D. degree from the University of Sherbrooke, Canada. He is the Chair Professor with Westlake University, Hangzhou, China; and a Emeritus Professor with Polytechnique Montréal, Canada. He is the Founder and the Director of the Center of Excellence in Biomedical Research on Advances-on-Chips Neurotechnologies (CenBRAIN Neurotech), Westlake University, Hangzhou; and the Polystim Neurotech Laboratory, Polytechnique Montréal. He has published more than 1000 peer-reviewed papers, one

handbook, three books, 13 book chapters, and 12 patents and 20 other patents are pending. He is a fellow of the Canadian Academy of Engineering, the Engineering Institutes of Canada, and the Asia-Pacific Artificial Intelligence Association (AAIA); and an "Officer" of the National Order of Quebec. He received several awards, among them the most prestigious and first Polytechnique Montréal Research and Innovation Award, the J. A. Bombardier and Jacques-Rousseau Awards from the ACFAS, the Queen Elizabeth II Golden Jubilee Medal, the Medal of Merit from the President of Lebanon, the Barbara Turnbull Award from the Canadian Institutes of Health Research (CIHR), the Shanghai International Collaboration Award, the Zhejiang Westlake Friendship Award, and the Qianjiang Friendship Ambassador Award. He is the Founder of the flagship IEEE International NEWCAS Conference and the Co-Founder of the International IEEE-BioCAS and IEEE-AICAS Conferences. He was the General Chair hosting both the 2016 IEEE International Symposium on Circuits and Systems (ISCAS) and the 2020 IEEE International Medicine, Biology and Engineering Conference (EMBC). He was awarded the Canada Research Chair in Smart Medical Devices from 2001 to 2015; and was leading the Microsystems Strategic Alliance of Quebec (ReSMiQ), Canada, from 1999 to 2018. He is the Co-Founder and an Associate Editor and was the Editor-in-Chief of the IEEE TRANSACTIONS ON BIOMEDICAL CIRCUITS AND SYSTEMS from 2016 to 2019.



**Benoit Gosselin** (Member, IEEE) received the Ph.D. degree in electrical engineering from the École Polytechnique de Montréal in 2009. He was an NSERC Post-Doctoral Fellow with the Georgia Institute of Technology in 2010. He is currently a Full Professor with the Department of ECE, Université Laval, where he holds the Canada Research Chair in Smart Biomedical Microsystems. His research interests include wireless microsystems for brain computer interfaces, analog/mixed-mode and RF integrated circuits for neural engineering, interface circuits of

implantable sensors/actuators, and point-of-care diagnostic microsystems for personalized healthcare. He served on the committees of several international IEEE conferences including BIOCAS, NEWCAS, EMBC, LSC, and ISCAS. Currently, he is leading the organization of the 20th NEWCAS Conference, which will be hosted in Quebec City, in June 2022. His significant contribution to biomedical microsystems research led to commercializing the first wireless microelectronic platform to perform optogenetics and electrophysiology in parallel with his partner Doric Lenses Inc. He is a fellow of the Canadian Academy of Engineering and he has received several prestigious awards, including NSERC Brockhouse Canada Prize and the Prix Génie Innovation of the Quebec professional engineering association OIQ. He is an Associate Editor of the IEEE TRANSACTIONS ON BIOMEDICAL CIRCUITS AND SYSTEMS and is the Chair and the Founder of the IEEE CAS/EMB Quebec Chapter (2015 Best New Chapter Award).